Astronomy & Astrophysics manuscript no. sn2011dh-2-v1
December 18, 2013

SN 2011dh - Understanding a Type IIb Supernova and its progenitor star.

M. Ergon[1], J. Sollerman[1], M. Fraser[2], A. Pastorello[3], S. Taubenberger[4], N. Elias-Rosa[5], M. Bersten[6], A. Jerkstrand[2], S. Benetti[3], M.T. Botticella[7], C. Fransson[1], A. Harutyunyan[8], R. Kotak[2], S. Smartt[2], S. Valenti[3], F. Bufano[9,10], E. Cappellaro[3], M. Fiaschi[3], A. Howell[11], E. Kankare[12], L. Magill[2,13], S. Mattila[12], R. Naves[14], P. Ochner[3], J. Ruiz[15], K. Smith[2], L. Tomasella[3], and M. Turatto[3]

[1] The Oskar Klein Centre, Department of Astronomy, AlbaNova, Stockholm University, 106 91 Stockholm, Sweden
[2] Astrophysics Research Center, School of Mathematics and Physics, Queens University Belfast, Belfast, BT7 1NN, UK
[3] INAF, Osservatorio Astronomico di Padova, vicolo dell'Osservatorio n. 5, 35122 Padua, Italy
[4] Max-Planck-Institut für Astrophysik, Karl-Schwarzschild-Str. 1, D-85741 Garching, Germany
[5] Institut de Ciències de l'Espai (IEEC-CSIC), Facultat de Ciències, Campus UAB, E-08193 Bellaterra, Spain.
[6] Kavli Institute for the Physics and Mathematics of the Universe, Todai Institutes for Advanced Study, University of Tokyo, 5-1-5 Kashiwanoha, Kashiwa, Chiba 277-8583, Japan
[7] INAF-Osservatorio Astronomico di Capodimonte, Salita Moiariello, 16 80131 Napoli, Italy
[8] Fundación Galileo Galilei-INAF, Telescopio Nazionale Galileo, Rambla José Ana Fernández Pérez 7, 38712 Breña Baja, TF - Spain
[9] INAF, Osservatorio Astrofisico di Catania, Via Santa Sofia, I-95123, Catania, Italy
[10] Departamento de Ciencias Fisicas, Universidad Andres Bello, Av. Republica 252, Santiago, Chile
[11] Las Cumbres Observatory Global Telescope Network, 6740 Cortona Dr., Suite 102, Goleta, CA 93117
[12] Tuorla Observatory, Department of Physics and Astronomy, University of Turku, Väisäläntie 20, FI-21500 Piikkiö, Finland
[13] Isaac Newton Group, Apartado 321, E-38700 Santa Cruz de La Palma, Spain
[14] Observatorio Montcabrer, C Jaume Balmes 24, Cabrils, Spain
[15] Observatorio de Cántabria, Ctra. de Rocamundo s/n, Valderredible, Cantabria, Spain

Submitted to Astronomy and Astrophysics

ABSTRACT

We present optical and near-infrared (NIR) photometry and spectroscopy of the Type IIb supernova (SN) 2011dh spanning ∼2 years and modelling of the bolometric lightcurve using hydrodynamical modelling for diffusion phase (3-40 days) and early tail (40-100 days) and steady-state NLTE modelling for the late tail (100-750 days). The fitting procedure for the hydrodynamical modelling is quantified by the use of a model grid spanning a large volume of paramater space which also allow us to determine the sensitivity of the results to errors in the observed quantities as well as a doing a consistent comparison of the derived quantities to SNe 1993J and 2008ax. The results are in good agreement with our results from (Bersten et al. 2012) and for SNe 1993J and 2008ax we find similar values although the mass of ^{56}Ni is sensitive to the adopted extinction and extinction. We also extend the temporal coverage of the model grid to 300 days using a correction for the flux outside the observed wavelength range determined with steady-state NLTE modelling. Applying this to SN 2011dh we find results in good agreement with those based on the 3-100 days bolometric lightcurve. Steady-state NLTE modelling of the 100-750 days bolometric lightcurve using a restricted set of ejecta models gives a reasonable fit to observations up to ∼400 days whereas the subsequent evolution cannot be reproduced. Time-dependent NLTE modelling shows that in this late phase freeze-out in the helium zone becomes important and a steady-state assumption is no longer valid. We find an excess in the MIR and NIR as compared to model photometry which could be explained by a modest amount of dust ($\tau = 0.2$) being formed in the ejecta, although the evolution after ∼400 days is not well reproduced. This amount of dust is also needed to reproduce the change in optical and near-infrared decline rates seen between ∼100 and ∼200 days. Comparisons of SNe 2011dh, 1993J and 2008ax show strong similarities and many of the differences could be explained by different masses and radii of the hydrogen rich envelope. The initial masses of $\lesssim$15 $M_\odot$ found by steady-state NLTE modelling of nebular spectra in Jerkstrand et al. (2013) and hydrodynamical modelling of the bolometric lightcurve in this paper suggests that all of these SNe originates from binary systems, which have been previously established for SN 1993J.

Key words. supernovae: general — supernovae: individual (SN 2011dh) — galaxies: individual (M51)

1. Introduction

Type IIb supernovae (SNe) are observationally characterized by a transition from Type II (with hydrogen lines) at early times to Type Ib (without hydrogen lines but with helium lines) at later times. The physical interpretation is that these SNe arise from stars that have lost most of their hydrogen envelop, either through stellar winds or interaction with a binary companion. Which of these production channels are dominating is still debated but for SN 1993J, the prime example of such an SNe, a companion star was detected by direct observations (Maund et al. 2004). The evolution of this binary system has been successfully modelled (Podsiadlowski et al. 1993; Stancliffe & Eldridge 2009) and it is widely accepted that the companion was

reponsible for the removal of the hydrogen envelope. Bright, nearby Type IIb SNe as 1993J, 2008ax and the recent 2011dh are essential to improve our understanding of this class. Observations of the progenitor star in pre-explosion images, a search for the companion star when the SN has faded and multi-method modelling of high quality data all provide important clues to the nature of Type IIb SNe and their progenitor stars.

In this paper we present our extensive optical and near-infrared (NIR) dataset, covering nearly two years, we have obtained for SN 2011dh. The first 100 days of this dataset have earlier been presented in Ergon et al. (2013, herafter E13). Detailed hydrodynamical modelling of the SN using those data were presented in Bersten et al. (2012, hereafter B12) and steady-state NLTE spectral modelling using late time data in Jerkstrand et al. (2013, hereafter J13). Identification and analysis of the plausible progenitor star have been presented in Maund et al. (2011, hereafter M11) and confirmation of the progenitor identification through its disappearence in E13.

SN 2011dh was discovered on 2011 May 31.893 UT (Griga et al. 2011) in the nearby galaxy M51 at a distance of 7.8 Mpc (E13). The SN has been extensively monitored from X-ray to radio wavelengths by several teams. Most observations cover the 3-100 days period but late time data have been published in Tsvetkov et al. (2012), Van Dyk et al. (2013), Sahu et al. (2013), Shivvers et al. (2013) and Helou et al. (2013). As in E13 we will focus on the UV to MIR emission. The explosion epoch, the distance to M51 and the interstellar line-of-sight extinction towards the SN used in this paper are all adopted from E13.

The nature of the progenitor star has been a key issue since the identification of a yellow supergiant in pre-explosion images coincident with the SN (M11; Van Dyk et al. 2011). Recent progress in modelling of the SN (B12; J13; Shivvers et al. 2013) and the disappearence of the progenitor candidate (E13; Van Dyk et al. 2013) strengthens the hypothesis that the progenitor was a yellow supergiant of moderate mass, as was originally proposed in M11. In this paper we present further modelling in support of this hypothesis. As shown in Benvenuto et al. (2013) a binary interaction scenario that reproduces the observed and modelled properties of the yellow supergiant is possible. HST observations that could detect or set useful constaints on the presence of a companion star are scheduled for Cycle 21.

The paper is organized as follows. In Sect. 2 we present the observations and describe the reduction and calibration procedures and in Sect. 3 we present an observational analysis and comparison of the observations to SNe 1993J and 2008ax. In Sect. 4 we model the bolometric lightcurve and in Sect. 5 we discuss the interpretation of the observations given our optimal model and discuss and review the results obtained so far and our current understanding of Type IIb SNe. Finally, we conclude and summarize the paper in Sect. 6. In Appendix A we provide details on the hydrodynamical modelling.

2. Observations

2.1. Software

As in E13 two different software packages have been used for 2-D reductions, measurements and calibrations of the data. The IRAF based QUBA pipeline (Valenti et al. 2011, hereafter V11) and another IRAF based package which we will refer to as the SNE pipeline. This package has been developed with the particular aim to provide the high level of automation needed for large sets of data.

2.2. Imaging

An extensive campaign of optical and NIR imaging was initiated for SN 2011dh shortly after discovery using a multitude of different instruments. The observations for during the first 100 days have been described in E13. The late time data have been obtained with the Liverpool Telescope (LT), the Nordic Optical Telescope (NOT), Telescopio Nazionale (TNG), the Calar Alto 3.5m and 2.2m telescopes, the Asiago 67/92cm Schmidt and 1.82m Copernico telescopes, the William Herschel Telescope (WHT), the Albanova Telescope (AT) and the United Kingdom Infrared Telescope (UKIRT). The major contributors were the NOT, the Asiago 67/92cm Schmidt and the AT for the optical observations and the the Calar-Alto 3.5m, the WHT and the UKIRT for the NIR observations. The late time dataset includes 61 epochs of optical imaging and 9 epochs of NIR imaging which, together with the early time observations, gives a total of 146 epochs of optical imaging and 32 epochs of NIR imaging.

2.2.1. Reductions and calibration

The optical and NIR raw data have been reduced with the QUBA and SNE packages respectively as described in E13, except for the optical LT and NIR UKIRT data for which reductions provided by the automated telescope pipelines have been used. Photometry was performed with the SNE pipeline as described in E13. Comparison to photometry on template subtracted images shows that the background contamination is negligible before ~300 days after which we have used photometry on template subtracted images. The optical and NIR photometry was calibrated to the Johnson-Cousins (JC), Sloan Digital Sky Survey (SDSS) and 2 Micron All Sky Survey (2MASS) systems as described in E13 where we also discuss the related uncertainties. The photometry was transformed to the standard systems using S-corrections (Stritzinger et al. 2002) except for the JC U and SDSS u bands which were transformed using the linear colour-terms tabulated in E13. As discussed in E13 we find the calibration to be accurate to within five percent in all bands for the first 100 days. The accuray of the late time photometry depends critically on the accuracy of the S-corrections. The late time JC and SDSS phototry were mainly obtained with the NOT but comparison between S-corrected NOT, LT and Calar-Alto 2.2m JC and SDSS observations at ~300 days show differences at the 5 percent level suggesting that this precision is maintained. We note that at this phase S-corrections are abolutely neccesary, for example the difference between the NOT and Calar-Alto I band observations are almost one magnitude at ~300 days if these are not applied, mainly because of the strong Ca II 7291,7323 and 8498,8542,8662 Å lines. The late time 2MASS photometry was obtained with a number of different telescopes and although the sampling is sparse the shape of the lightcurves suggest that errors in the S-corrections are modest. Note that we have used JC-like $UBVRI$ filters and SDSS-like gz filters at NOT whereas we have used JC-like BV filters and SDSS-like $ugriz$ filters at LT and FTN. The JC-like URI and SDSS-like uri photometry were then tied to both the JC and SDSS systems to produce full sets of JC and SDSS photometry.

2.2.2. Space Telescope Observations

We have also performed photometry on the Spitzer 3.6 and 4.5 μm imaging[1] and the SWIFT optical and UV imaging. For the

[1] Obtained through the DDT program by G. Helou.

Spitzer imaging we performed aperture photometry using the SNE pipeline as described in E13 to calculate magnitudes in the natural (energy flux based) Vega system of IRAC as well as JC UBV using S-corrections. All Spitzer images were template subtracted as described in E13. Optical and UV SWIFT magnitudes were published in E13 where we also provide details on the reductions.

2.2.3. Results

The S-corrected optical and NIR magnitudes and their corresponding errors are listed in Tables 4, 5 and 6 and the Spitzer 3.6 and 4.5 μm magnitudes and their corresponding errors in Table 7. For simplicity we also include the magnitudes for the first 100 days already published in E13. All magnitudes including the SWIFT magnitudes published in E13 are shown in Fig. 1 which also shows cubic spline fits using 3-5 point knot separation, error weighting and a 5 percent error floor. The standard deviation around the fitted splines is less than 5 percent and mostly less than a few percent except for the SWIFT $UVM2$ band for which the standard deviation is between 5 and 10 percent on the tail. All calculations in Sect. 3, including the bolometric lightcurve, are based on these spline fits. In these calculations the errors have been estimated as the standard deviation around the fitted splines and then propagated.

2.3. Spectroscopy

An extensive campaign of optical and NIR spectroscopic observations was initiated for SN 2011dh shortly after discovery with data obtained from a multitude of telescopes. The observation during the first 100 days have been described in E13. The late time data have been obtained with the NOT, the TNG, the WHT, the Calar Alto 2.2m telescope, the Asiago 1.22m Galileo telescopes and the Gran Telescopio Canarias (GTC). The major contributors were the NOT, the WHT and the GTC. Details of all spectroscopic observations, the telescope and instrument used, epoch and instrument characteristics are given in Table **??**. The late time dataset includes 18 optical spectra obtained at 13 epochs and 2 NIR spectra obtained at 2 epochs which, together with the early time observations, gives a total of 73 optical spectra obtained at 39 epochs and 20 NIR spectra obtained at 12 epochs.

2.3.1. Reductions and calibration

The optical and NIR raw data were reduced and the flux extracted using the QUBA and SNE pipelines respectively as described in E13. The optical and NIR spectra were flux and wavelength calibrated using the QUBA and SNE pipelines respectively as described in E13. The absolute flux scale of all spectra has been calibrated against interpolated photometry using a least square fit to all bands for which the mean energy wavelength is at least half an equivalent width within the spectral range.

2.3.2. Results

All reduced, extracted and calibrated spectra will be made available for download from the Weizmann Interactive Supernova data REPository[2] (WISeREP) (Yaron & Gal-Yam 2012). Figure 3 shows the sequence of observed spectra where those obtained on the same night using the same telescope and instrument have been combined. For clarity, and as is motivated by the frequent sampling of spectra, all subsequent figures in this and the following sections are based on time-interpolations of the spectral sequence as described in E13. To further visualize the evolution, the spectra have been aligned to a time axis at the right border of the panels. Interpolated spectra were also used in the calculations of the bolometric lightcurve (Sect. 3.3) and S-corrections. Figure 2 shows the interpolated optical and NIR spectral evolution of SN 2011dh for days 5−425 with a 20-day sampling. All spectra in this and subsequent figures spectra have been corrected for redshift and interstellar extinction.

[2] http://www.weizmann.ac.il/astrophysics/wiserep/

3. Analysis

In this section we provide an observational analysis and comparison to the Type IIb SNe 1993J and 2008ax. Beside SN 2011dh these are the best monitored Type IIb SNe sofar which motivates a detailed comparison. Both occured in nearby galaxies, have progenitor detections and well constrained explosion epochs. As discussed in E13 the systematic errors stemming from the uncertainty in distance and extinction are large for all three SNe which should be kept in mind when absolute quantities are compared. For SNe 1993J and 2008ax we adopt the same values and error bars for the distance and extinction as in E13. The references for the photometric and spectroscopic data of SNe 1993J and 2008ax used in the comparison are the same as specified in E13.

3.1. Photometric evolution

Absolute magnitudes were calculated as in E13. In Fig. 4 we show absolute optical and NIR magnitudes for SN 2011dh as compared to SNe 1993J and 2008ax and in Table 1 we tabulate the time and absolute magnitude of the maximum, and the tail decline rates at 100, 200 and 300 days. Most striking is the similarity between the three SNe except for a shift, which as discussed in E13 could be explained by an error in the adopted extinction. Another difference is the early evolution, where the lightcurves of SN 1993J show a decline before ∼10 days. Such a decline is also seen in the lightcurves of SN 2011dh before ∼3 days (not shown here but see A11 and T12) whereas there is only a hint of this behavior in the lightcurves of SN 2008ax. Except for this, the behavior is most similar showing a strong increase in luminosity from day 3 to the peak followed by a decrease down to a tail with a roughly linear decline rate. The maximum occurs at increasingly later times for redder bands. The drop from the maximum down to the tail is more pronounced for bluer bands and is not seen for bands redder than I.

Except for the early tail the optical decline rates are fairly constant for all three SNe, being roughly twice the decay rate of ^{56}Co. For SN 2001dh all decline rates except for the K band tend to decrease at later times, which also seems to be the case for SNe 1993J and 2008ax. The J and H band decline rates are considerably higher than the optical at 100 days for all three SNe, being three or even four times the decay rate of ^{56}Co. For SNe 2011dh and 1993J these have decreased considerably at 200 days and for SN 2011dh these are lower than the optical at 300 days. The K band decline rate is a considerably lower than the J and H band decline rates for SNe 2011dh and 1993J at 100 days but is considerably higher than the J and H band decline rates at 300 days for SN 2011dh. Between 450 and 700 days the optical lightcurves of SN 2011dh flattens and the decline rates decrease considerably, approaching the decay rate of ^{56}Co.

Contrary to SNe 1993J and 2008ax, SN 2011dh was also monitored in UV and MIR. As seen in Fig. 1 the Swift $UVM2$

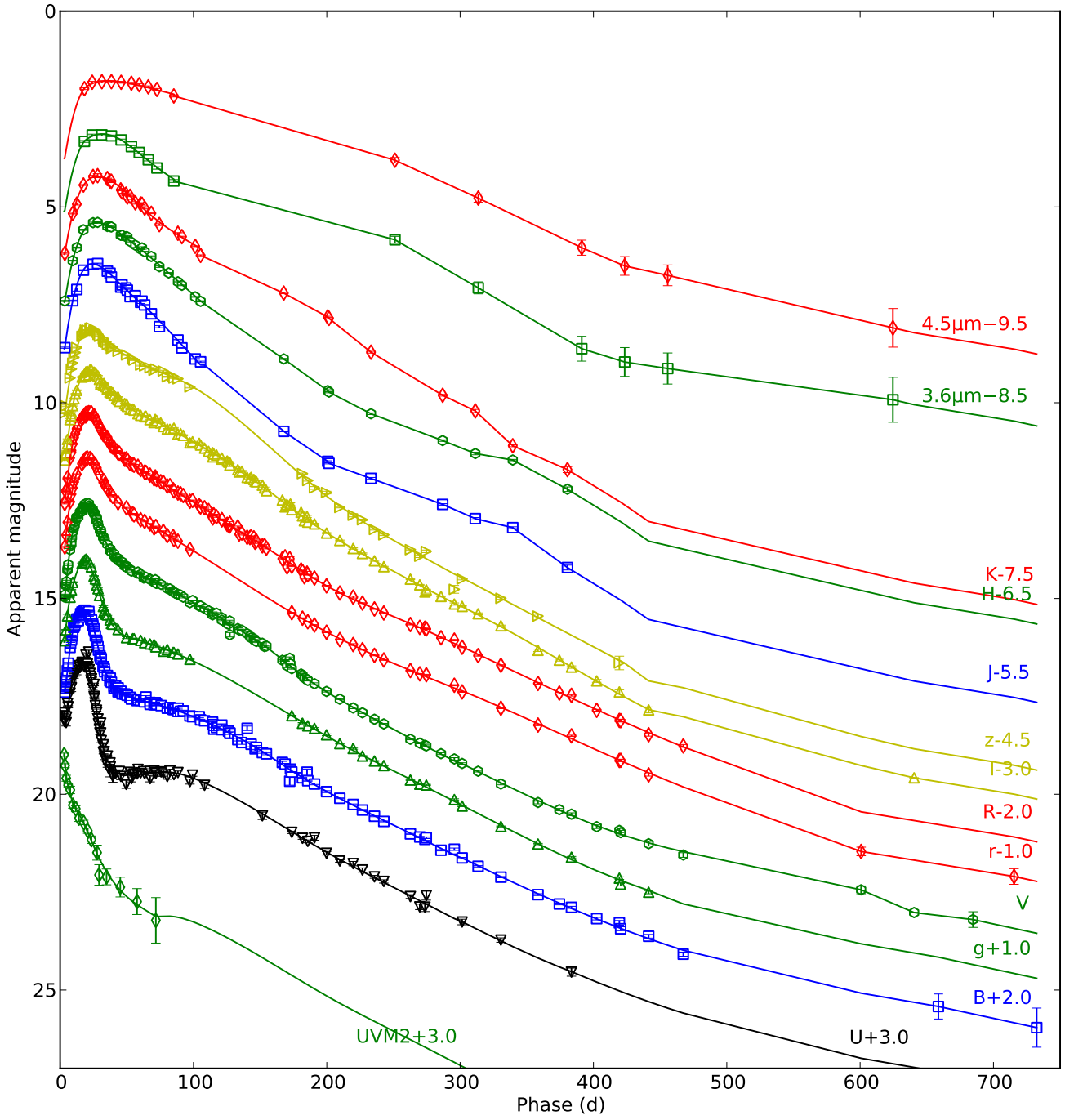

Fig. 1. Photometric evolution of SN 2011dh in the UV, optical, NIR and MIR. For clarity each band has been shifted in magnitude. Each lightcurve has been annotated with the name of the band and the shift applied. We also show the S-corrected SWIFT JC photometry (crosses) and cubic spline fits (solid lines).

band shows a quite different evolution than the other bands with a monotonic strong decrease between 3 and 80 days. The Spitzer 3.6 and 4.5 μm bands follows a similar evolution as the other bands for the first 100 days although, as discussed in E13, the 4.5 μm shows a considerably slower decline than the 3.6 μm and the NIR bands. Later on, a strong excess in both the Spitzer bands develops between 100 and 250 days. Between 250 and 400 days the decline rates are fairly constant and similar to the optical bands but between 400 and 700 days the Spitzer lightcurves flatten and the decline rates decrease considerably in a way similar to the optical bands.

3.2. Colour evolution and blackbody fits

Figure 5 shows the intrinsic *U*-*V*, *B*-*V*, *V*-*R*, *V*-*I*, *V*-*J*, *V*-*H* and *V*-*K* colour evolution of SN 2011dh as compared to SNe 1993J and 2008ax. This is essentlially the lighturves normalized to the *V* band and is a way of visualising the distribution of the flux within the SED. The similarity between the three SNe is striking except for a shift, which could be explained by an error in the adopted extinction (E13). For SN 2011dh we see an initial quite strong blueward trend in the *V*-*R* to *V*-*K* colours reaching a minimum at ~10 days which is not reflected in the *U*-*V* and *B*-*V* colours. SN 1993J shows a similar behaviour although the trend

Table 1. Times and absolute magnitudes of the maximum and tail decline rates at 100, 200, 300 and 400 days for SN 2011dh as compared to SNe 1993J and 2008ax as measured from cubic spline fits.

SN	Band	Maximum (days)	Magnitude (mag)	Rate (100 d) (mag day^{-1})	Rate (200 d) (mag day^{-1})	Rate (300 d) (mag day^{-1})	Rate (400 d) (mag day^{-1})
2011dh	*U*	18.01	-16.16	0.013	0.019	0.018	...
2011dh	*B*	19.01	-16.43	0.014	0.019	0.017	0.015
2011dh	*V*	20.01	-17.08	0.018	0.021	0.018	0.015
2011dh	*R*	21.43	-17.38	0.020	0.019	0.016	0.016
2011dh	*I*	22.43	-17.41	0.019	0.021	0.017	0.020
2011dh	*J*	24.51	-17.57	0.036	0.017	0.012	...
2011dh	*H*	27.51	-17.60	0.029	0.019	0.011	...
2011dh	*K*	27.51	-17.76	0.020	0.020	0.024	...
1993J	*U*	18.39	-17.32	0.006	...	...	...
1993J	*B*	20.39	-17.09	0.011	0.017	0.012	...
1993J	*V*	22.39	-17.47	0.019	0.019	0.017	...
1993J	*R*	21.39	-17.72	0.022	0.015	0.013	...
1993J	*I*	22.39	-17.72	0.022	0.019	0.013	...
1993J	*J*	23.80	-17.93	0.041	0.016	...	...
1993J	*H*	22.80	-17.88	0.033	0.018	...	...
1993J	*K*	22.80	-18.04	0.023	0.022	...	...
2008ax	*U*	16.70	-18.55	0.013	...	...	...
2008ax	*B*	19.78	-18.04	0.015	0.018	0.016	...
2008ax	*V*	21.78	-18.15	0.022	0.018	0.017	...
2008ax	*R*	21.71	-18.17	0.023	0.016	0.015	...
2008ax	*I*	22.71	-18.13	0.018	0.021	0.013	...
2008ax	*J*	22.81	-17.90	0.035	...	...	...
2008ax	*H*	23.81	-17.93	0.032	...	...	...
2008ax	*K*	23.81	-18.03	0.033	...	...	...

starts later (at the luminosity minimum) and the colour minimum is reached later (at ∼20 days). Before ∼10 days all the colours of SN 1993J show a redward trend. For SN 2008ax there is no NIR coverage before ∼10 days but all other colours shows the blueward trend. For SN 2011dh the blueward trend is followed by a redward trend reaching a maximum at ∼40 days. Both SNe 1993J and 2008ax show a very similar behavior.

For SN 2011dh the evolution after the colour maximum is slow and quite diverse among the colours. This is not surprising as in this phase the SED becomes more and more dominated by lines and the colours mainly reflect the evolution of these. Until ∼150 days the evolution is fairly consistent though and all colours except *V*-*I* shows blueward trends of varying strength. After ∼150 days the *U*-*B* and *B*-*V* colours shows weak blue trends, the *V*-*R* colour shows a redward trend reaching a colour maximum at ∼350 days and then a blueward trend, the *V*-*I* colour stays nearly constant until ∼350 days and then shows a blueward trend, the *V*-*J* and *V*-*K* colours show redward trends and the *V*-*K* colour shows a redward trend reaching a colour maximum at ∼250 days and then a blueward trend. Both SNe 1993J and 2008ax show quite similar behavior in all colours. Notable exceptions are the *V*-*I* colour for 2008ax which is not constant and the *V*-*J* to *V*-*K* colours for SN 1993J which do not show the redward trends seen in SN 2011dh.

In E13 we discussed the blackbody temperature and radius for SN 2011dh as inferred from fits the *V*, *I*, *J*, *H* and *K* bands. Such fits only have physical meaning during the early phase when the approximation of a blackbody emitting surface is valid. In E13 we did not show a comparison with SNe 1993J and 2008ax though. Fig. 6 show the blackbody temperature for the first 100 days for SN 2011dh as compared to SNe 1993J and 2008ax as well as the systemetic errors arising from the errors in extinction. Apparently SN 2008ax is much hotter than SNe 2011dh and 1993J for the adopted extinction.

3.3. Bolometric evolution

As in E13 we have used a combination of the spectroscopic and photometric methods, applied to wavelength regions with and without spectral information respectively, when calculating the bolometric lightcurves. The details of these methods have been described in E13.

Figure. 7 shows the U to K (3300-24000 Å) bolometric lightcurve as calculated with the photometric method for SN 2011dh as compared to SNe 1993J and 2008ax for day 0-500. For SN 2011dh the U to K bolometric lightcurve shows a strong increase in luminosity from 3 days to peak luminosity at 20.45 days followed by a decrease down to a tail with a roughly linear decline rate. The decline rate on the tail is 0.020 mag day^{-1} at 100 and 200 days and decrease to 0.016 and 0.015 mag day^{-1} at 300 and 400 days, respectively. There is however a significant increase in the decline rate between 150 and 200 days that breaks this pattern. The data from the first three days published in A11 and T12 are insufficient to construct a bolometric lightcurve but it is clear that this phase corresponds to a strong decline of the bolometric luminosity. The U to K bolometric lightcurves of

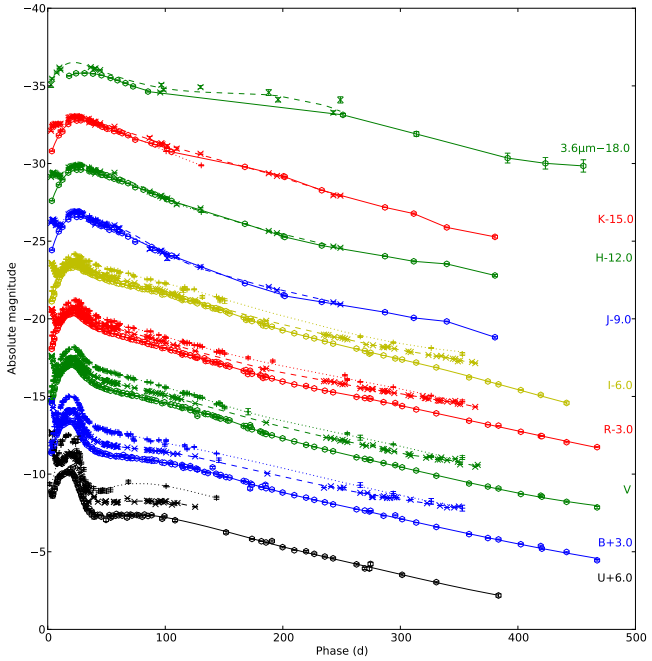

Fig. 4. Photometric evolution of SN 2011dh in the optical and NIR as compared to SNe 1993J and 2008ax. For clarity each band has been shifted in magnitude. Each lightcurve has been annotated with the name of the band and the shift applied.

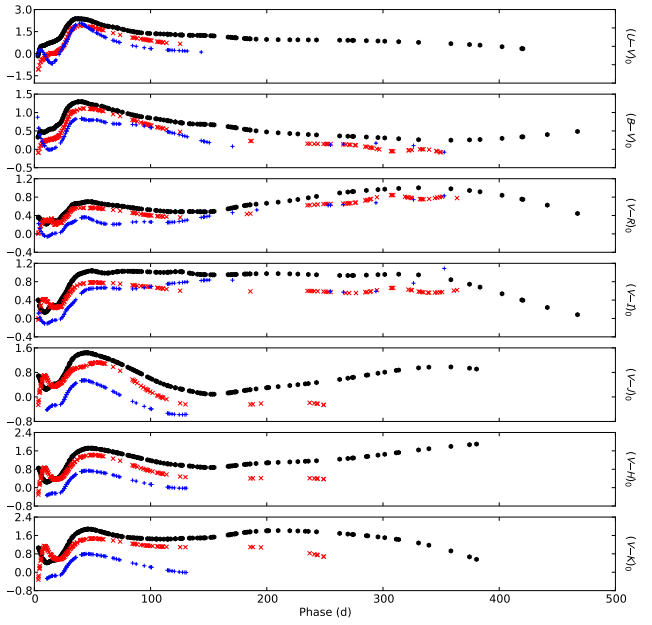

Fig. 5. *U-V*, *B-V*, *V-R*, *V-I*, *V-J*, *V-H* and *V-K* intrinsic colour evolution for SN 2011dh (black dots) as compared to SNe 1993J (red triangles) and 2008ax (blue squares.

SNe 1993J and 2008ax both have larger luminosities as well as larger peak-to-tail luminosity ratios. As discussed in E13 both these differences could be explained by an error in the extinction. Given this and the caveat that SNe 1993J and 2008ax are not covered in NIR after ∼250 and ∼150 days respectively, their U to K bolometric lightcurves are remarkably similar to the one of SN 2011dh. There are however some differences. For SN 2008ax the intial decline is not seen although there is a hint in

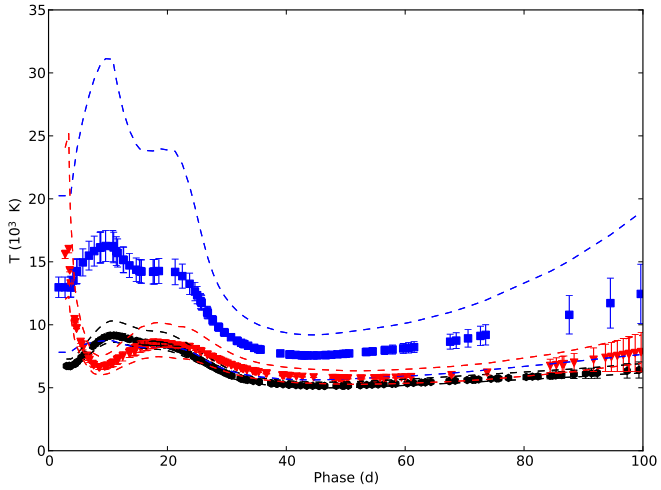

Fig. 6. Evolution of the blackbody temperature for SN 2011dh (black dots) as inferred from fits to the *V*, *I*, *J*, *H* and *K* bands compared to SNe 1993J (red crosses) and 2008ax (blue pluses). We also show the systematic errors arising from the errors in extinction (dashed lines).

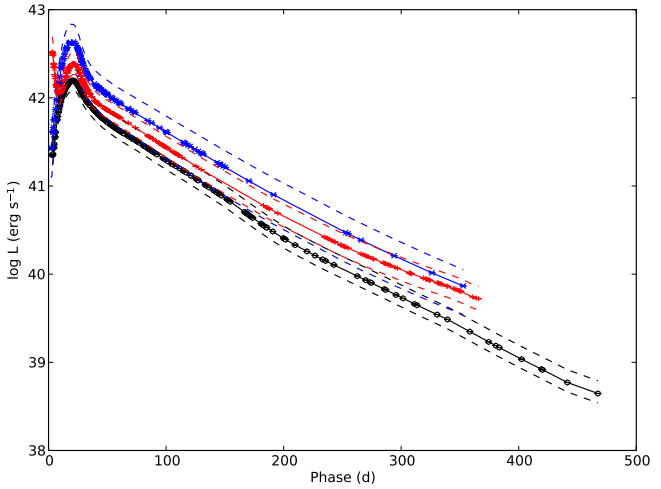

Fig. 7. Pseudo-bolometric U to K lightcurve for SN 2011dh (black circles and solid line) calculated with the photometric method as compared to SNe 1993J (red crosses and solid line) and 2008ax (blue pluses and solid line). The upper and lower error bars for the systematic error arising from extinction and distance (dashed lines) are also shown.

the early *U* band observations. For SN 1993J the initial decline is slower and lasts for ∼10 days and the decline rates at 200 and 300 are increasingly lower. Neither SN 1993J nor SN 2008ax shows the increase in decline rate at 150-200 days.

The 3-732 days UV to MIR (1900-50000 Å) pseudo-bolometric lightcurve as calculated with the combined spectroscopic and photometric methods is shown in Figure. 8 and the 3-300 days period (for which we have full UV to MIR coverage) listed in Table 9 for reference. As expected the UV to MIR lightcurve is very similar to the U to K lightcurve. The decline rates at 100, 200, 300 and 400 days are 0.021, 0.022, 0.015 and 0.016 mag day^{-1} but the increase in decline rate between 150 and 200 days is not as pronounced. Given the caveat that the NIR coverage ends at ∼350 days and the sampling is sparse and the measurement errors large after ∼500 days the UV to MIR lightcurve show a significant flattening after ∼500 days where

Table 2. Times and luminosity of the maximum and tail decline rates at 100, 200, 300 and 400 days for the U to K bolometric lightcurve of SN 2011dh as compared to SNe 1993J and 2008ax.

SN	Maximum (days)	Luminosity (log(erg s^{-1}))	Rate (100 d) (mag day^{-1})	Rate (170 d) (mag day^{-1})	Rate (200 d) (mag day^{-1})	Rate (300 d) (mag day^{-1})	Rate (400 d) (mag day^{-1})
2011dh	20.89	42.19	0.021	0.024	0.021	0.016	0.017
2008ax	21.30	42.63	0.020	0.019	0.017	0.015	...
1993J	21.43	42.38	0.021	0.019	0.017	0.013	...

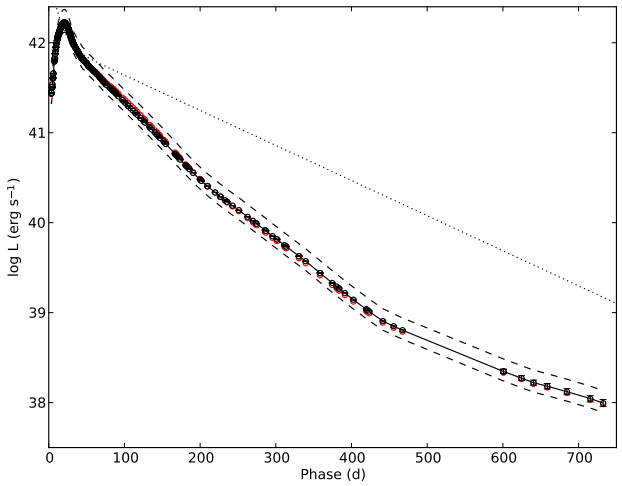

Fig. 8. Pseudo-bolometric UV to MIR lightcurve for SN 2011dh calculated with the spectroscopic (black circles and solid line) and photometric (red circles) method. The upper and lower error bars for the systematic error arising from extinction and distance (black dashed lines) and the radioactive decay chain luminosity of 0.075 $M_\odot$ of ^{56}Ni (black dotted line) are also shown.

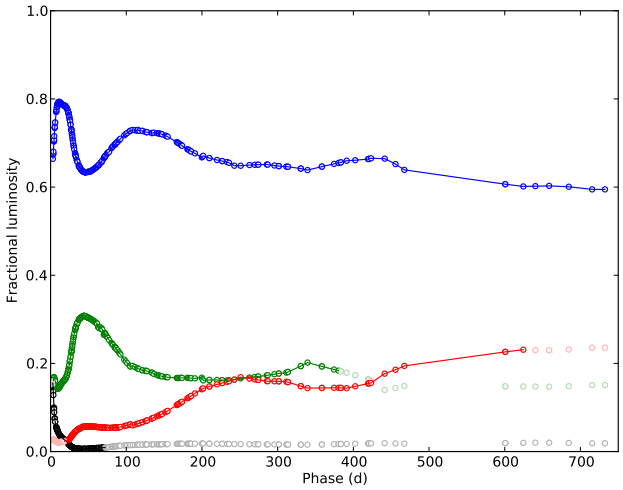

Fig. 9. Fractional UV (black dots), optical (blue dots), NIR (green dots) and MIR (red dots) luminosity for SN 2011dh. The fractional Rayleigh-Jeans luminosity redwards of 4.5 μm (red dashed line) is also shown for comparison.

the decline rate decrease to a value slightly lower than the decay rate of ^{56}Co.

Figure. 9 shows the fractional UV (1900-3300 Å), optical (3300-10000) Å), NIR (10000-24000 Å) and MIR (24000-50000 Å) luminosities for SN 2011dh for day 0-750. The optical flux dominates and varies between ∼60 and ∼80 percent. The NIR fraction varies between ∼15 and ∼30 percent, the MIR fraction between a few and ∼25 percent and the UV fraction between ∼1 and ∼15 percent. Between ∼3 and ∼10 days (corresponding to the colour minimum) we see a strong increase in the optical fraction and a strong decrease in the UV fraction whereas the NIR fraction stays roughly constent. Between ∼10 and ∼40 days (corresponding to the colour maximum) we see a strong decrease in the optical fraction, a continued strong decrease in the UV fraction and a strong increase in the NIR and MIR fractions. Between ∼40 and ∼100 days we see an increase in the optical fraction and a decrease in the NIR fraction wheras the UV and MIR fractions stay roughly constant. Between ∼100 and ∼200 days we see a decrease in the optical and NIR fractions and a strong increase in the MIR fraction. The subsequent evolution becomes quite uncertain after ∼350 days where the NIR coverage ends and ∼500 days where the sampling and measurement errors becomes worse, but the optical, NIR and MIR fractions seems to stay roughly constant during this period.

3.4. Spectroscopic evolution

The early spectral evolution was discussed in some detail in E13 and in this section we will focus on the spectral evolution from 100 days and onwards. Steady-state NLTE modeling of our spectra in this phase as well as a detailed analysis of the formation of the identified lines and the evolution of their fluxes are presented in J13. In this section we will summarize the findings in J13 and expand the analysis to the line profiles and what can be learned about the distribution of material in the different nuclear burning zones. In doing this we will refer to the subdivision of the ejecta according to J13 with a Fe/Co core surrounded by the Si/S zone, the oxygen-rich O/Si/S, O/Ne/Mg and O/C zones, the helium-rich H/C and H/N zones and the hydrogen-rich envelope. The amount of macroscopic mixing between these zones is determined by hydrodynamical instabilities in the explosion and is a free parameter in the steady-state NLTE modelling.

In Sect. 3.4.1 we will describe different methods for characterization of the line profiles, in Sect. 3.4.2-3.4.8 we will discuss the identified lines element by element, in Sect. 3.4.10 we will discuss small scale variations in the line profiles and in Sect. 3.4.11 we will compare the line profiles of SN 2011dh to those of SNe 1993J and 2008ax.

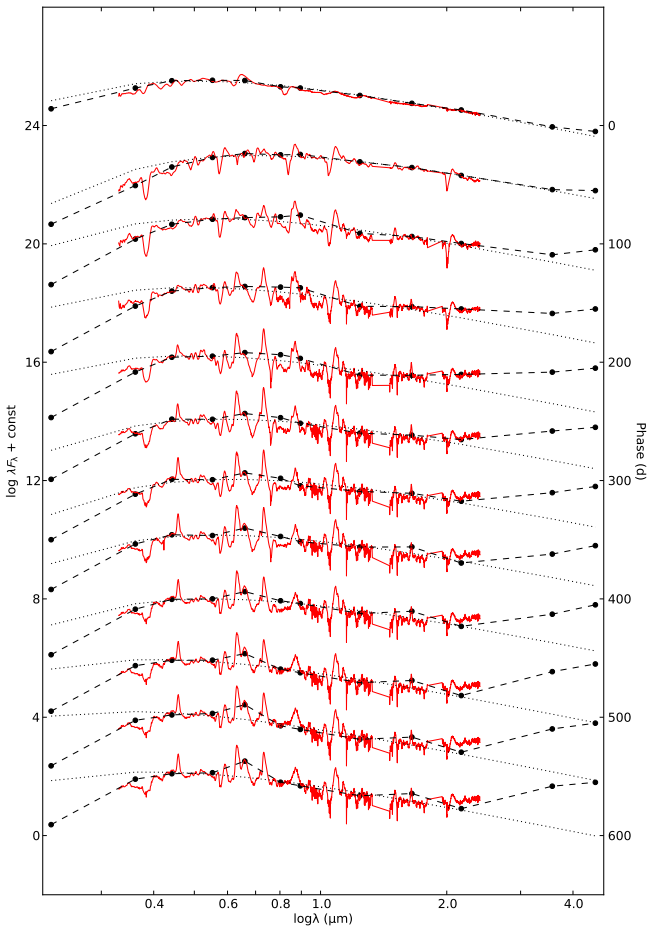

Fig. 10. The evolution of the SED as calculated with the photometric method (black dots and dashed lines) overplotted with the blackbody fits discussed in Sect. 3.2 (black dotted lines) as well as the observed spectra interpolated as described in Sect. 2.3.2 (red solid lines).

3.4.1. Line profile characterization

We have used a number of different methods to characterize the line profiles. First we have used a purely observational (except for identification) method which calculates the typical wavelength and widths of the lines. The typical wavelength of the line is estimated as the first wavelength moment of the flux (center of flux) and the typical widths as the blue- and red-side regions containing 76 percent of the flux, corresponding to the half-width-half-maximum (HWHM) for a gaussian profile. Both these quantities are quite unsensitive to the continuum subtraction and are thus suitable for characterization and comparison to other SNe. The continuum level was determined in a way similar to what was done in J13 by a linear interpolation between the minimum flux levels on the blue and red sides within a region set to ±6000 km s^{-1} for most of the lines, ±10000 km s^{-1} for the Ca II 8662 line and ±3000 km s^{-1} for the [Fe II] 7155 Å line.

Fig. 11 shows the center of flux velocities and blue- and red-side widths as compared to the rest wavelength for the [O I] 6300,6364, O I 5577, Mg I] 4571, Na I 5890,5896 [Ca II] 7291,7323, Ca II 8498,8542,8662 and the [Fe II] 7155 Å lines as estimated with this method. The rest wavelength was set to 6316 Å for the [O I] 6300,6364 line Å line as appropriate for a line ratio of 3.0 and to 5993, 7307 and 8662 Å for the Na I 5890,5896 [Ca II] 7291,7323, Ca II 8498,8542,8662 lines respectively.

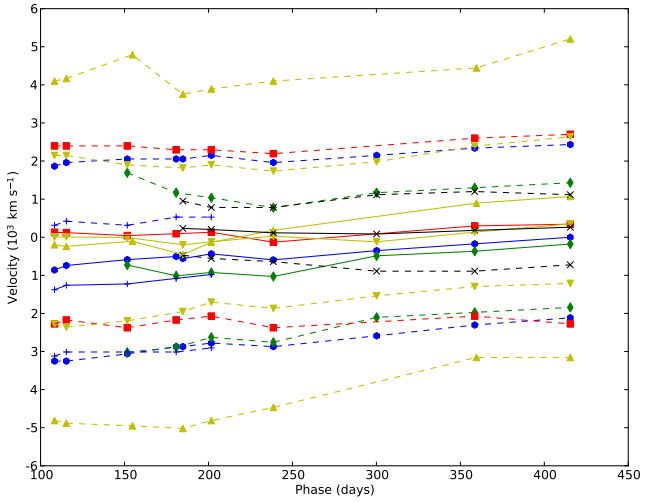

Fig. 11. Center of flux velocities (solid lines) and the blue- and red-side widths (dashed lines) as compared to the rest wavelengths for the [O I] 6300,6364 (black dots), Mg I 4571 (blue diamonds), Na I 5890,5896 (green squares), [Ca II] 7291,7323 (red downward triangles), Ca II 8498,8542,8662 (yellow uppward triangles) and the [Fe II] 7155 (black crosses) Å lines.

Secondly, we have used a method partly based on the knowledge gained from the modelling in J13 to estimate the sizes of the line emitting regions and the optical depths required to cause the blue-shift of the typical wavelength seen in many lines. This issue is discussed in some detail in J13 were the physical cause of this blue-shift is suggested to be line-blocking in the core. For lines found to be optically thin using the NLTE modelling we fit the line profile of a sphericaly symmetric region of constant line emissivity, optically thin in the line and with a constant absorptive opacity to the observed line profile. This gives a rough estimate of the size of the region responsible for bulk of the line emission. Some lines arise as a blend of more than one line and for these we have applied different methods to take this into account. For the [O I] 6300,6364 line we have assumed a line ratio of 3.0 as is supported by the steady-state NLTE modelling and estimates based on small scale variations (Sect. 3.4.10). In other case were such information is not available we have made a simulataneous fit assuming the same size of the emitting region for all of the blended lines.

3.4.2. Hydrogen lines

Summary of the findings in J13: No (isolated) hydrogen lines are identified. Some Hα emission arising from the hydrogen-rich envelope is present but is found to be increasingly dominated by [N II] 6548,6583 Å emisson arising from the helium zone from ∼150 days and onwards. No detectable absorption is found in Hα or any other of the hydrogen lines.

The right panel of Fig. 12 shows the post 100 days (interpolated) spectral evolution centred on the Hα line. There is a dip in the [O I] 6300,6364 Å line profile after ∼150 days that corresponds well to the early time Hα absorption minimum at ∼11000 km s^{-1} (E13). However, as discussed in Sect. 3.4.10 this feature repeats in a number of other lines and is rather due to clumping/assymetries in the ejecta.

After ∼200 days there is an emerging emission feature near the rest wavelength of Hα which, as mentioned above, is found to arise mainly from the [N II] 6548,6583 Å line by the steady-

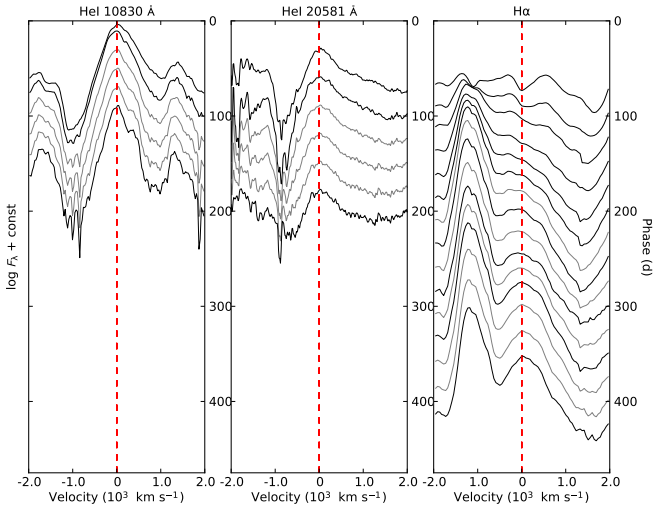

Fig. 12. Closeup of (interpolated) spectral evolution centred on the He I 10830 Å (left panel), He I 20581 Å (middle panel) and Hα (right panel) lines.

state NLTE modelling in J13. Using the method described in Sect. 3.4.1 we find the feature to be well fitted by emission from a region with a radius of 5500 km s^{-1} emitting mainly in the [N II] 6583 Å line, although the wings of the observed line profile may extend to ∼12000 km s^{-1} on the red side. Hα emission from the hydrogen-rich envelope would be expected to result in a box-like line profile, at least 11000 km s^{-1} wide (E13). The size of the line emitting region, as well as the extent of the wings, is instead consistent with emission from the helium zone in agreement with the results in J13.

!But the peak at late times is exactly at the rest wavelength of Hα. What does this mean?!

3.4.3. Helium lines

Summary of the findings in J13: The (isolated) helium lines identified are the He I 10830 and 20581 Å lines although the He I 10830 Å line is found to be blended with the [S I] 10820 Å line. The helium lines arise mainly from the helium zone but there is also a significant contribution from helium in the Fe/Co zone. Both lines are found to be optically thick implying a significant contribution from line scattering.

The left and middle panels of Fig. 12 shows the post 100 days (interpolated) spectral evolution for the identified helium lines. The helium lines emerge between ∼10 and ∼15 days and, except for the He I 10830 and 20581 Å lines, fades away or dissapears due to blending with other lines towards ∼100 days. The He I 10830 and 20581 Å lines however, stays strong until our last NIR spectrum at ∼200 days, both in emission and absorption.

Both the He I 10830 and 20581 Å lines have distinct P-Cygni like line profiles suggesting a significant contribution from scattering in agreement with the results from J13. Although the unblended He I 20581 Å line has a quite broad peak it is not flat-topped suggesting a contribution from helium at low velocities. This is again in agreement with the results from J13 where we find helium in the F/Co zone to contribute signicicantly at low velocities.

3.4.4. Oxygen lines

Summary of the findings in J13: The (isolated) oxygen lines identified are the O I 5577, 7774, 9263, 11300 and 13164 and the [O I] 6300,6364 Å lines although the O I 9263 Å line is found to be blended with the [Co II] 9338,9344 Å line on the blue side. All these lines are found to arise from the oxygen zones, the part arising from the O/C and O/Si/S zones depending sensitively on the cooling from molecule (CO and SiO) emission. The O I 5577 and [O I] 6300,6364 Å lines arise from low lying states which is found to be thermally populated whereas the O I 7774, 9263, 11300, and 13164 Å lines arise from higher lying states which is found to be populated by recombinations.

Fig. 13 shows the post 100 days (interpolated) spectral evolution for the identified oxygen lines. The O I 5577, 7774, 9263, 11300 and 13164 Å lines all emerge between ∼25 and ∼50 days. After ∼100 days the [O I] 6300,6364 Å line emerge as well and stays strong until our last spectrum at ∼400 days. The O I 5577 Å line disappears after ∼300 days, the O I 7774 Å line starts to decline after ∼200 days but is still visible in our last optical spectrum at ∼400 days wheras the O I 11300, and 13164 Å lines seems to be still rising in our last NIR spectrum at ∼200 days.

Using the method described in Sect. 3.4.1 we measure the radius of the [O I] 6300,6364 line emitting region to 3400, 3100 and 2900 km s^{-1} at 202, 300 and 415 days respectively. The line profile fit is quite good but the observed emission is underestimated at low velocities and extends to at least ∼5000 km s^{-1} suggesting radially decreasing emissivity.

As seen in Fig. 11 the center of flux for the [O I] 6300,6364 Å line (assuming a line ratio of 3.0) shows a blue-shift of ∼1000 km s^{-1} gradually decreasing towards zero at ∼400 days and the center of flux for the O I 5577 Å line shows a blue-shift of ∼1500 km s^{-1} at ∼100 days gradually decreasing towards ∼1000 km s^{-1} at ∼200 days when the line disappears. Using the method described in Sect. 3.4.1 we find the blue shift of the [O I] 6300,6364 Å line to correspond to an absorptive optical depth in the line emitting region of 0.4, 0.3 and 0.1 at 202, 300 and 415 days respectively. This is in agreement with the results in J13 where the cause of this blue-shift is found to be line-blocking. We don't find any blue-shift of the O I 11300 and 13164 Å lines where we expect line-blocking to be less effective in support of this hypothesis.

3.4.5. Sodium lines

Summary of the findings in J13: The only (isolated) sodium line identified is the Na I 5890,5896 Å line. Observationally this line is hard to disentangle from the He I 5876 line but the emission is found to arise mainly from the Na I 5890,5896 Å line (although absorption could be a blend) and to be a combination of recombination emission from the O/Ne/Mg zone and scattering throughout the ejecta.

The right panel of Fig. 14 shows the post 100 days (interpolated) spectral evolution for the Na I 5890,5896 Å line. The feature shows a distinct P-Cygni like line profile suggesting a significant contribution from scattering in agreement with the results from J13 and stays strong, both in emission and absorption, until our last spectrum at ∼400 days.

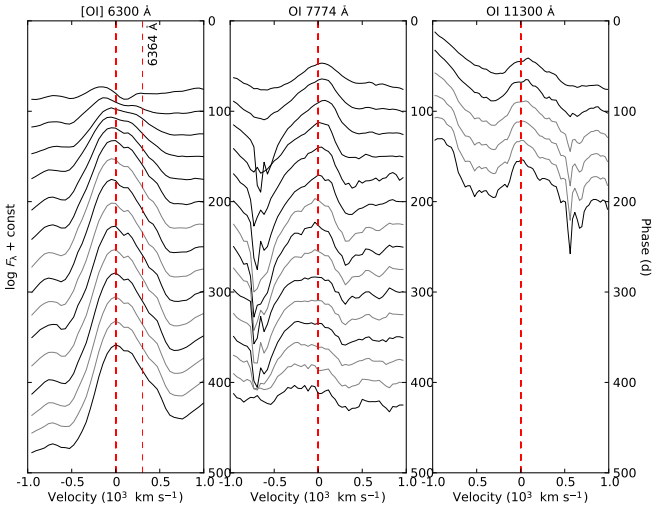

Fig. 13. Closeup of (interpolated) spectral evolution centred on the [O I] 6300,6364 Å (left panel), O I 7774 Å (middle panel) and O I 11300 Å (right panel) lines.

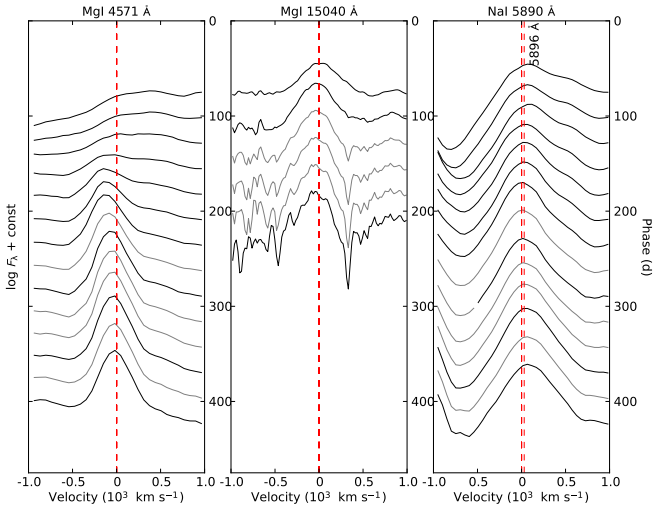

Fig. 14. Closeup of (interpolated) spectral evolution centred on the [Mg I] 4571 Å (left panel), Mg I 14050 Å (middle panel) and Na I 5890,5896 Å (right panel) lines.

3.4.6. Magnesium lines

Summary of findings in J13: The (isolated) magnesium lines identified are the Mg I] 4571 and the Mg I 15040 Å lines. Those lines are found to arise mainly from the O/Ne/Mg zone and the parent states to be poplulated mainly by recombinations although the low lying parent state of the Mg I] 4571 line may have a significant contribution from thermal excitations.

The left and middle panels of Fig. 14 show the post 100 days (interpolated) spectral evolution for the identified magnesium lines. The Mg I] 4571 Å line emerges at ∼150 days and stays strong until our last optical spectrum at ∼400 days. The Mg I 15040 Å line emerges at ∼40 days and stays strong until our last NIR spectrum at ∼200 days.

Using the method described in Sect. 3.4.1 we measure the radius of the Mg I] 4571 line emitting region to 3600, 2800 and 2700 km^{-1} at 202, 300 and 415 days respectively. We also measure the radius of the Mg I] 15040 Å line emitting region to 3400 and 2900 km^{-1} at 89 and 205 days respectively. The line profile fit of the Mg I] 4571 Å line is quite good but the observed emission is underestimated at low velocities and extends to at least ∼5000 km s^{-1} suggesting radially decreasing emissivity.

As seen in Fig. 11 the center of flux for the Mg I] 4571 Å line shows a blue-shift of ∼1000 km s^{-1} at ∼200 days decreasing towards a few hundred km s^{-1} at ∼400 days. Using the method described in Sect. 3.4.1 we find the blue shift of the Mg I] 4571 Å line to correspond to an absorptive optical depth in the line emitting region of 1.2, 0.8 and 0.3 at 202, 300 and 415 days respectively. This is in agreement with the results from J13 where the cause of this blue-shift is found to be line-blocking. We don't find any significant blue-shift in the Mg I 15040 Å line (!Verify this!) where we expect line-blocking to be less effective in support of this hypothesis.

The estimated radius of the Mg I line emitting region of 2700-3600 km s^{-1} is similar to the estimated radius of the O I line emitting region of 2900-3400 km s^{-1}. As mentioned above, in J13 the Mg I lines is found to arise from the O/Ne/Mg zone and the O I lines to arise from the O/Ne/Mg zone and, depending on the amount of molecule emission, the O/C and O/Si/S zones. The profiles of the [O I] 6300 and the Mg I] 4571 Å lines as well as small scale variations in these (Sect. 3.4.10) are very similar suggesting these to arise from the same nuclear burning zone.

3.4.7. Calcium lines

Summary of the findings in J13: The (isolated) calcium lines identified are the Ca II 3934,3968, 8498,8542,8662 and [Ca II] 7291,7323 Å lines. Absorption in the Ca II 3934,3968 Å lines is found to occur throughout the ejecta and the Ca II 8498,8542,8662 Å lines to arise mainly from fluorescence in these lines. The [Ca II] 7291,7323 Å lines on the other hand, seem to arise mainly from the Si/S zone with a possible contribution throughout the ejecta from fluorescence in the Ca II 3934,3968 Å lines.

Fig. 15 shows the post 100 days (interpolated) spectral evolution for the identified calcium lines. The Ca II 3934,3968 and 8498,8542,8662 Å lines are both present initially in strong P-Cygni profiles whereas the [Ca II] 7291,7323 Å line emerges at ∼100 days. The Ca II 8498,8542,8662 Å lines disappears in absorption at ∼100 days, and the Ca II 8498,8542 Å lines in emission at ∼300 days. After ∼100 days the Ca II 8662 Å line declines but stays rather strong until our last optical spectrum at ∼400 days. The Ca II 3934,3968 Å line stays strong in absorption and the [Ca II] 7291,7323 Å line in emission until our last optical spectrum at ∼400 days.

Using the method described in Sect. 3.4.1 we measure the radii of a two-component [Ca II] 7291,7323 line emitting region to 2400/9900, 2100/9100 and 2400/9000 km s^{-1} with a line ratio of 1.3, 1.2 and 0.5 at 202, 300 and 415 days respectively. The line profile fit is good in the inner region but worse in the wings which are quite assymetric and also blended with the [Fe II] 7155 on the blue side. The more pronounced red-side wing could indicate a P-Cygni like contribution from scattering.

The size of the inner [Ca II] 7291,7323 line-emitting region of 2100-2400 km s^{-1} is less than the 2700-3600 km s^{-1} found for the Mg I and O I line emitting regions which, assuming this emission arise mainly from the Si/S zone (see above), suggests partial mixing of the Si/S zone and the surrounding oxygen zones. The size of the outer [Ca II] 7291,7323 line-emitting region of 9000-

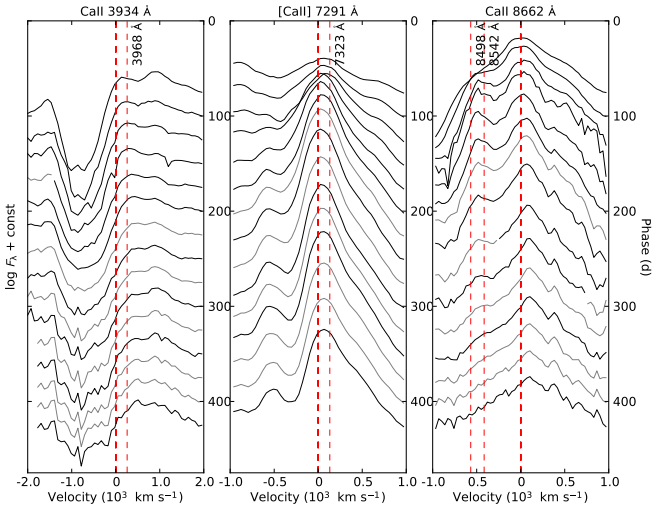

Fig. 15. Closeup of (interpolated) spectral evolution centred on the Ca II 3934/3968 Å (left panel), [Ca II] 7291/7323 Å (middle panel) and Ca II 8498/8542/8662 Å (right panel) lines.

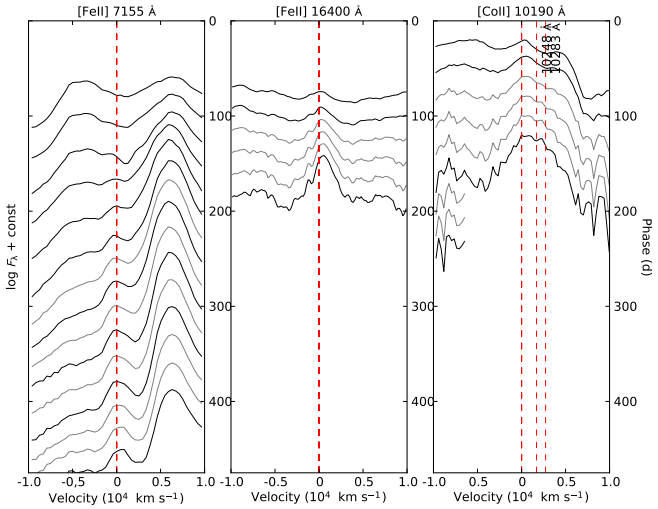

Fig. 16. Closeup of (interpolated) spectral evolution centred on the [Fe II] 7155 Å (left panel), [FeII II] 16400 Å (middle panel) and [Co II] 10190,10248,10283 Å (right panel) lines.

9900 km s^{-1} implies a contribution from calcium in the helium zone.

3.4.8. Iron group lines

Summary of the findings in J13: The (isolated) iron lines identified are the [Fe II] 7155, 12600 and 16400 Å lines. Numerous lines from Fe II and Fe I are also found to be the main source of the quasi-continuum bluewards ∼6000 Å emerging at ∼100 days. The (isolated) cobalt lines identified are the [Co II] 9338,9344, 10190,10248,10283 and 15475 Å lines, although the [Co II] 9338,9344 Å line is found to be blended with the O I 9263 Å line on the blue side. All of the identified iron and cobalt lines are found to arise from the Fe/Co zone.

Fig. 16 shows the post 100 days (interpolated) spectral evolution for the identified iron lines. The [Fe II] 7155 Å line emerges at ∼150 days and the [Fe II] 12600 and 16400 Å lines are seen in our last NIR spectrum at ∼200 days. The [Fe II] 7155 Å line persists until our last optical spectrum at ∼400 days.

Using the method described in Sect. 3.4.1 we measure the radius of the [Fe II] 7155 Å line emitting region to 1600 km s^{-1} at 300 and 415 days and the radius of the [Fe II] 16440 Å line emitting region to 2100 km^{-1} at 206 days.

Fig. 17 shows the post 100 days (interpolated) spectral evolution for the identified cobalt lines. The [Co II] 9338,9344 Å line may emerge as early as ∼50 days and persists until our last spectrum covering this region at ∼300 days whereas the [Co II] 10190,10248,10283 and the 15475 Å lines are seen in our last NIR spectrum at ∼200 days.

Using the method described in Sect. 3.4.1 we measure the radius of the [Co II] 10190,10248,10283 Å line emitting region to 1800 and 2000 km s^{-1} at 89 and 206 days respectively. The [Co II] 15475 Å line is noisy but we find the radius of the line-emitting region to be 3200 km s^{-1} at 206 days. As mentioned the [Co II] 9338,9344 Å line is blended with the O I 9263 Å line on the blue side and also appears to be blended with other lines on the red side so we do not attempt to estimate the radius of the line emitting region.

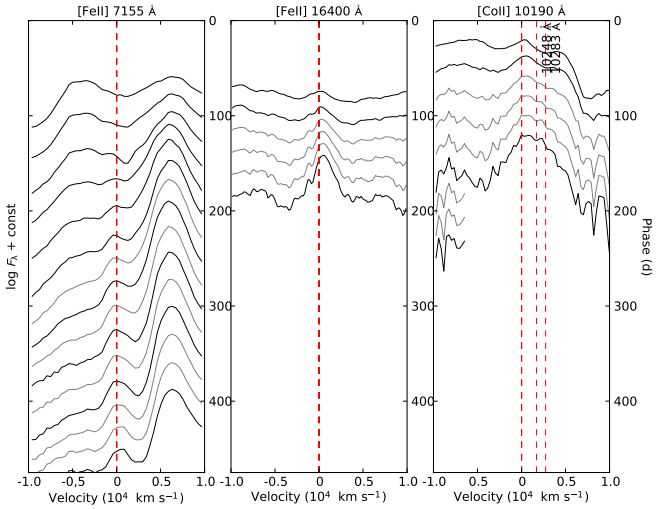

Fig. 17. Closeup of (interpolated) spectral evolution centred on the [Fe II] 7155 Å (left panel), [FeII II] 16400 Å (middle panel) and [Co II] 10190,10248,10283 Å (right panel) lines.

Except for the [Co II] 15475 Å line at 206 days the estimates of the size of the Fe II and Co II line emitting region lies in the range 1600-2100 km s^{-1}, significantly smaller than the 2700-3600 km s^{-1} estimated for the O I and Mg I line emitting region. This is consistent with a scenario where the Fe/Co core and the sourrounding oxygen zones are only partially mixed. However, as discussed in Sect. 4.5, hydrodynamical modelling of the early lightcurve strongly suggest that some amount of Fe/Co core material have been mixed far out in the ejecta. This is not neccesarily in conflict with the Fe II and Co II line profiles as the amount of material mixed far out in the ejecta may be small enough not to be clearly visible.

3.4.9. CO overtone band

Figure. 18 shows the continuum subtracted flux between 22750 and 24350 Å were we expect CO overtone band emission. The continuum was estimated as a linear interpolation between the

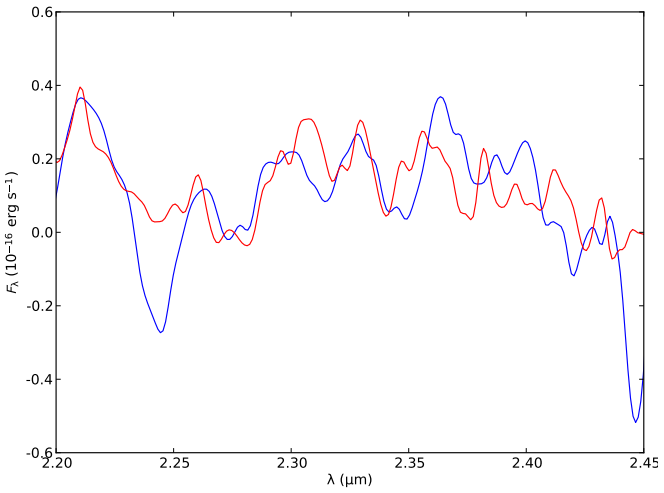

Fig. 18. Continuum subtracted CO overtone region at 88 days (blue) and 206 days (red). The flux at 206 days have been scaled with the ratio of the measured total fluxes in the region.

averaged 22700-22800 Å and 24300-24400 Å regions. The integrated continuum subtracted flux was 2.2×10^{-14} and 5.7×10^{-15} erg s^{-1} cm^{-2} at 88 and 206 days respectively.

The total flux in the 4.5 μm band, calculated using the zero-point flux and the equivalent width of the band was 4.9×10^{-13} and 1.7×10^{-13} erg s^{-1} cm^{-2} at 88 and 206 days respectively. Note that the value at 206 days lies in the gap of the Spitzer observations and has been linearly interpolated between 85 and 251 days. If all of the flux in the 4.5 μm band was due to CO fundamental band emission this would correspond to fundamental to overtone band flux ratios of ∼20 and ∼30 at 85 and 206 days respectively.

3.4.10. Small scale fluctuations

Figure. 19 shows small scale fluctuations in the [O I] 6300,6364, O I 5577, O I 7774, Mg I 4571 and Na I 5890,5896 Å lines at 202 and 300 days. The resolution is ∼600 and ∼250 km s^{-1} in the 202 and 300 days spectra respectively. A 1000 km s^{-1} box average of the line profile was repeatedly (3 times) subtracted to enhance the smal scale fluctuations. In the upper left panel we show a comparison of the [O I] 6300 Å line profiles at 202 and 300 days. These are very similar and there is not much evolution of the small scale fluctuations in the line profile during this period. We identify 9 features marked A-H with an FWHM between 300 and 600 km s^{-1} present at both epochs.

However, features G and H interpreted as belonging to the [O I] 6364 line match very well with the E and F features interpreted as belonging to the [O I] 6300 Å line profile so these are likely to be repetitions. We have corrected the [O I] 6300 Å line profile for the contamination from the [O I] 6364 Å line assuming that the [O I] 6364 Å line dominates the region redwards 3000 km s^{-1} and the [O I] 6300 Å line dominates the region bluewards -500 km s^{-1}. Minimizing the difference between the observed flux and $F_{6300}(v) + F_{6364}(v - \Delta v) = (F_{blue}(v) + RF_{red}(v - \Delta v)) + (F_{blue}(v) + RF_{red}(v - \Delta v))/R$ where R is the [O I] 6300,6364 line ratio and Δv the [O I] 6300,6463 Å velocity difference gives a very good fit and line ratios of 2.3 and 2.6 at 202 and 300 days respectively. These line ratios are in reasonable agreement with the 3.0 expected for optically thin emission.

In the upper right panel we show the [O I] 6300 Å line profile corrected by subtraction of the [O I] 6364 Å line profile estimated from the fit. In the lower left panel we show a comparison of the corrected [O I] 6300 Å line profile and the Mg I 4571 Å line profile at 300 days. All features except B are clearly identified and the agreement is very good. In the lower right panel we show a comparison of the corrected [O I] 6300 line profile and the O I 5577, O I 7774, and Na I 5890/5896 Å line profiles at 202 days. The E and F features are clearly identified in all of these line profiles but none of the other features are seen. Since the E and F features are also the strongest it is not clear if the abscence of the other features is real or if the other features are just too faint to be seen.

Shivvers et al. (2013) presented an analysis of the line profiles of the [O I] 6300,6364, O I 7774 and Mg I 4571 Å lines at 268 days. By decomposition of the [O I] 6300 Å line profile into gaussian profiles assuming a [O I] 6300,6364 Å line ratio of 3.0 they found a good fit for one broad and two narrow profiles located at -400 and 1600 km s^{-1}. The two strongest features in our analysis, E and F, are located at ∼0 and ∼1500 km s^{-1} and clearly correspond to the two features found by Shivvers et al. (2013). They also find these features to repeat in the O I 7774 and Mg I 4571 Å lines in agreement with our analysis. The difference in velocity for the blue feature is likely explained by the different methods used were our method surpress flux variations on scales larger than 1000 km s^{-1}.

Matthews et al. (2002) presented a similar analysis of the small scale fluctuations in the line profiles of SN 1993J. They found a good agreement between the [O I] 6300, 5577 and 7774 Å line profiles which is in agreement with our results for SN 2011dh if we assume that the fainter features are hidden in the noise of the [O I] 5577 and 7774 Å line profiles. However, they did not find a good agreement between the [O I] 6300 and Mg I 4571 line profiles which is a bit surprising since we find an excellent agreement between these line profiles. One possible explanation could be that the [O I] 6300 is dominated by flux from the O/Ne/Mg zone for SN 2011dh but not for SN 1993J as we expect the Mg I 4571 Å line emerge from this zone wheras the [O I] 6300 Å line could also have contributions from the O/Si/S and O/C zones. The contributions to different lines from different zones for SN 2011dh are discussed in detail in J13.

The small scale fluctuations observed provide evidence for a clumpy ejecta as have been previously demonstrated for SN 1993J (Matthews et al. 2002) and 1987A (Stathakis et al. 1991; Chugai 1994). Matthews et al. (2002) used the statistical model for a clumpy ejecta by Chugai (1994) to estimate a filling factor of ∼0.06 for oxygen zone material distributed within a sphere with 3800 km s^{-1} radius. Using their estimated typical clump size of 300 km s^{-1} this corresponds to ∼900 clumps. The model requires the radius of the sphere containing the clumps, the typical size of the clumps and the RMS of relative flux fluctuations in lines originating from the clumps. In the case of SN 2011dh we estimate the radius of the sphere containing the bulk of the O/Ne/Mg zone material to ∼3500 km s^{-1} from the widths of the [O I] 6300 Å and Mg I 4571 Å lines. For SN 1987A a typical cloud size of 120 km s^{-1} was estimated from the power spectrum of the [O I] 6300 Å line by Stathakis et al. (1991) using high-resolution spectroscopy but it is not clear how this was done by Matthews et al. (2002) although they had acces to high-resolution spectroscopy. As we have do not have access to high-resolution spectroscopy for SN 2011dh we can only estimate an upper limit on the typical cloud size taken to be 300 km s^{-1}, the

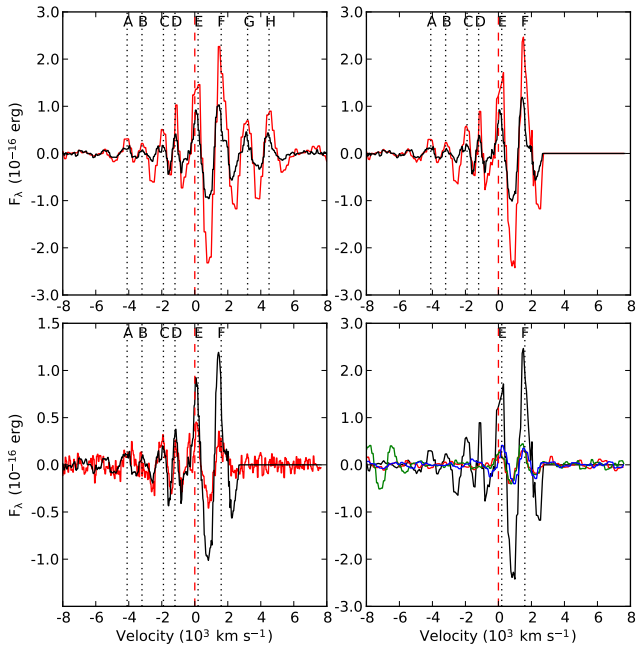

Fig. 19. Comparison of box average subtracted line profiles. The upper left panel shows the [O I] 6300 Å line profile at 202 (red) and 300 (black) days. The upper right panel shows the corrected [O I] 6300 Å line profile at 202 (red) and 300 (black) days. The lower left panel shows the corrected [O I] 6300 Å line profile (black) and the Mg I 4571 (red) Å line profile at 300 days. The lower right panel shows the corrected [O I] 6364 Å line profile (black) and the O I 5577 (red), O I 7774 (green), and Na I 5890/5896 (blue) Å line profiles at 202 days

smallest size of the features seen. The RMS of the flux fluctuations was calculated to ~0.09 in the inner part of the sphere from the [O I] 6300 Å line profile. Using these estimates and applying Chugai (1994, eq. 11) we get an upper limit on the filling factor of O/Ne/Mg zone material within the sphere of ~0.07 and a lower limit on the number of O/Ne/Mg zone clumps of ~900. These values are in good agreement with the values estimated by Matthews et al. (2002) for the clumping of oxygen zone material in SN 1993J.

3.4.11. Comparison to SNe 1993J and 2008ax

The early evolution was briefly compared in E13 with focus on the hydrogen and helium lines. In this section we focus on the evolution after ~100 days. Fig. 20 shows the (interpolated) spectral evolution centred on the [O I] 6300 Å, O I 7774 Å, He I 10830 and 20581 Å, Na I 5890,5896 Å, Mg I 4571 Å, [Fe II] 7155 and 16436 Å, [Ca II] 7291 Å and Ca II 8662 Å lines for SN 2011dh as compared to SNe 1993J and 2008ax.

The double peaked profiles of the [O I] 6300,6364 Å and the He I 10830 and 20581 Å lines for SN 2008ax have been previously discussed in Taubenberger et al. (2011), Maurer et al. (2010) and Milisavljevic & Fesen (2010). Maurer et al. (2010) used a steady-state NLTE code and a torus like distribution of helium to reproduce the He I 10830 and 20581 Å lines and suggested that scattering by Hα could be responsible for the double peaked profile of the [O I] 6300,6364 Å line wheras Milisavljevic & Fesen (2010) suggested a superposition of appropriate [O I] 6300 and 6364 Å line profiles as the separation of the peaks are close to the line separation of ~64 Å. However, as a number of other lines show similar double peaked or flat topped line profiles, we find none of these explanations convincing.

Fig. 21 shows the [O I] 7774 Å, O I 5577 Å, Na I 5890,5896 Å, He I 10830 and 20581 Å, Mg I 4571 and 15040 Å, [Ca II] 7291 Å and Ca II 8662 Å lines as compared to the [O I] 6300 Å line for SN 2008ax at 131 and 280 days. The Na I 5890,5896 Å line shows a profile most similar to the [O I] 6300,6364] Å, line at both 131 and 280 days. The [O I] 7774 Å line also shows a similar profile at 280 days whereas the line profile at 131 days is flat topped and has a flux deficit on the red side. The Mg I 4571 and 15040 Å lines shows flat topped profiles fairly similar to the [O I] 6300,6364 Å line but without double peaks at 131 days whereas the Mg I 4571 has a flux deficit on the red side at 280 days and the single peak is coincident with the blue peak of the [O I] 6300,6364] Å line. The O I 5577 Å line has a flux deficit on the red side and the single peak is coincident with the blue peak of the [O I] 6300,6364 Å line. The [Ca II] 7291 Å and Ca II 8662 Å lines shows a quite different behaviour and both have single peaked line profiles centred at their rest wavelengths. Finally, as is also shown in Fig. 21 the profiles of the [Fe II] 7155 and 16346 Å lines are clearly shifted to the blue peaking at ~1000 and extending to about ~5000 km s^{-1} with little emission on the red side

The good agreement between the [O I] 6300,6364 Å and the Na I 5890,5896 Å lines as well as the O I 7774 Å line at 280 days and the similar but broader double peaked structure seen in the He I 10830 and 20581 Å lines suggests that neither scattering in Hα nor a superposition of appropriate [O I] 6300 and 6364 Å line profiles is responsible for the double peaked structure of the [O I] 6300,6364 Å line. In J13 we do not find any significant scattering in Hα and the line ratio of [O I] 6300,6364 Å line is close to 3.0 at late times for SN 2011dh. We also note that the Mg I 4571 and O I 5577 Å lines showing a single peak coincident with the blue peak of the [O I] 6300,6364 both are located in a wavelengh region were we expect the line opacity to be large and, as is also shown in J13, emission from the receeding side of the SN could be blocked. The Mg I 15040 Å line at 131 days and the O I 7774 Å line at 280 days does not show a significant flux deficit on the red side.

The double-peaked and/or flat-topped profiles seen could be explained by a torus-line distribution of the the materal but other geometries are possible, A partially mixed ejecta preserving some of the onion-like structure of the nuclear burning zones with a core of mixed Fe/Co and Si/S material, the oxygen zone material residing outside ~2000 km s^{-1} and the helium zone material outside ~3000 km s^{-1} could explain the shape of most line profiles. The double-peaks could be explained by some amount of bipolar assymetry, the centrally peaked [Ca II] 7291 Å and Ca II 8662 Å lines by syntesized calcium in the Si/S zone and the blue-shifted [Fe II] 7155 and 16346 Å lines by an assymetric distribution of the Fe/Co material. The rather large volyme occupied by the core could be explained by expansion because of heating from the radioactive decay of ^{56}Ni.

There is a clear difference between the shape of the SN 2011dh and 2008ax line profiles. The flat-topped and double peaked profiles seen in SN 2008ax are not clearly seen in SN 2011dh although the [O I] 6300,6364 Å line has a weak double peaked shape to some extent repeated in other lines (Sect. 3.4.10). This difference could be explained by a different viewing angle if the structure of the ejecta is torus-like or has some amount of bipolar assymetry or there could be an intrinsic differ-

ence between the SNe. The line profiles of SN 1993J are somewhat intermediate in shape and have flatter line profiles as compared to SN 2001dh except for the [Ca II] 7291 Å and Ca II 8662 Å lines which have similar centrally peaked line profiles for all three SNe.

4. Modelling

In this section we discuss modelling of the bolometric and photometic lightcurves with the steady-state NLTE code used in J13 and described in Jerkstrand et al. (2011, 2012) and HDE, a new hydrodynamical code similar to the one used in B12 and described in Appendix A. In Sect. 4.1 we discuss modelling of the 0-500 days bolometric and photometric lightcurves with the steady-state NLTE code and the HDE code using the J13 ejecta models and in Sect. 4.2, 4.3 we discuss the effects on these lightcurves by dust absorption/emission and molecule emission. In 4.4 we discuss modelling of the 500-700 days bolometric lightcurves and the effects of time dependenent processes in this phase. In Sect. 4.5 we make a quantitative fit of the 0-100 days bolometric lightcurves of SNe 2011dh, 1993J and 2008ax using a model grid spanning a large volume of parameter space constructed with the hydrodynamical HDE code. In Sect. 4.6 we extend the temporal coverage of this model grid to 300 days and use a correction for the flux within the observed wavelength range determined by the steady-state NLTE modelling to fit the observed 3-300 days U to 4.5 μm pseuso-bolometric lightcurve of SN 2011dh.

4.1. Modelling of the bolometric lightcurve day 100-500

In this section we compare synthetic pseudo-bolometric lightcurves for the J13 ejecta models to the observed pseudo-bolometric lightcurves. For day 1-100 we use the HDE code setup to run in homologous mode. The temperature profile for the initial model is taken to be that of the optimal model found in Sect. 4.5. In the optimal model homology is reached and the thermal explosion energy gets exhausted at ~3 days so these assumptions are not critical for the subsequent evolution. For day 100-500 we calculate the bolomectric lightcurve from spectra modelled with the steady-state NLTE code and previously analysed in J13. The parameters of the ejecta models are given in table 2 in J13.

Figures 22 and 23 show a comparison of the U to 4.5 μm (3300-50000 Å) pseudo-bolometric lightcurves for day 0-500 and day 0-100 respectively calculated from the observed magnitudes and synthetic magnitudes for the J13 ejecta models. For day 0-100 we show the bolometric lightcurve as calculated with the HDE code and the 10-15 percent drop in luminosity at 100 days corresponds to the fraction of the luminosity outside the U to 4.5 μm wavelength range. Figures 24 show the same comparison for the U to z (3300-10000 Å) pseudo-bolometric lightcurve. This figure do not show the bolometric lightcurves calculated with the HDE code as the larger fraction of the luminosity outside the covered wavelength range would make such a comparison misleading.

The model giving the best fit to the U to 4.5 μ and U to z pseudo-bolometric lightcurves is model 12C which, as discussed in J13, is also the model giving the best fit to the spectral evolution. The models differ in one ore more of the following parameters, degree of macroscopic mixing (medium or strong), positron trapping (local or free-streaming), molecule cooling (yes or no), dust absorption/emission (yes or no) and oxygen zone filling factor (small or large). The optimal model (12C) has strong macroscopic mixing, local positron trapping, no molecule cooling, dust absorption/emission and small oxygen zone filling factor. The meaning of each parameter and the different configurations used are described in detail in J13. Here we will discuss the effect of changing these parameters on the pseudo-bolometric and photometric lightcurves.

The degree of macroscopic mixing affects the lightcurves in several ways. Most important is the mixing of the Fe/Co zone containing the ^{56}Ni synthesized in the explosion and its decay products, determining the deposition of the radioactive decay energy in the ejecta. The mixing of the other zones in turn determine the deposition of the radioactive decay energy in each of these zones. We have used two configurations, one where all core zones (Fe/Co-O/C) are randomly mixed within 3500 km s^{-1} and one that differs only in that 50 percent of Fe/Co material have been mixed out in the helium zone within 3500-6000 km s^{-1}. As compared to the optimal model (12C) all models with no Fe/Co material outside 3500 km s^{-1} show a slower rise to peak luminosity. In Sect. 4.5 we show that the optimal hydrodynamical model also has strong outward mixing of the ^{56}Ni which seems to be required to fit the rise to peak luminosity. As compared to the optimal model (12C) these models also have higher luminosity on the tail and in general do not give a good fit to the lightcurve. Clearly there is a large number of possible configurations that have not been investigated, e.g. a configuration with partial mixing of the core zones as we found evidence for in Sect. 3.4.

The filling factors of each macroscopically mixed zone affects the lightcurves mainly because the density of the zone affects the thermal cooling rates and the recombinations rates. Note that in the optically thin limit the deposition of radioactive decay energy is not changed as the total cross section of the zone remains the same. We have used two configurations where we have set the filling factor of the oxygen zones to a high and a low value and adjusted the filling factors of the other zones accordingly (see J13 for details on the filling factors). Again there is a large number of possible configurations that have not been investigated. Ideally, the effect of a change of the filling factor for each core zone would need to be investigated as well as configurations with multi-component filling factors (more than one density for the clumps from a given zone).

The positron trapping only affects the lightcurves when the fraction of radioactive decay energy deposited by the positrons becomes significant and before this models with locally trapped or free-streaming positrons are indistinguishable. As compared to the optimal model (12C) model 12B which differs only in that the positrons are free-streaming the decline rate in the optical bolometric lightcurve is much lower after 300 days. The reason for this is that in the optimal model (12C) all positrons are trapped in the Fe/Co zone and do not contribute to the heating of other zones, resulting in a lower luminosity in lines arising from these zones, in particular the [O I] 6300,6364 a and Mg I] 4571 Å lines. A slower decline rate is also seen in the U to MIR bolometric lightcurve, but only after ~400 days and the difference is less pronounced as the NIR luminosity in the optimal model (12C) is higher because of a large number of iron lines arising from the Fe/Co zone. The choice of local positron trapping for the optimal model (12C) is motivated by the better fit to the pseudo-bolometric lightcurves after ~300 days when the contribution from positrons to the deposited radioactive decay energy starts to become significant. We also note that the spectrum obtained at ~700 days (!Check this!) presented by Shivvers et al. (2013) shows a dramatic change as compared to our

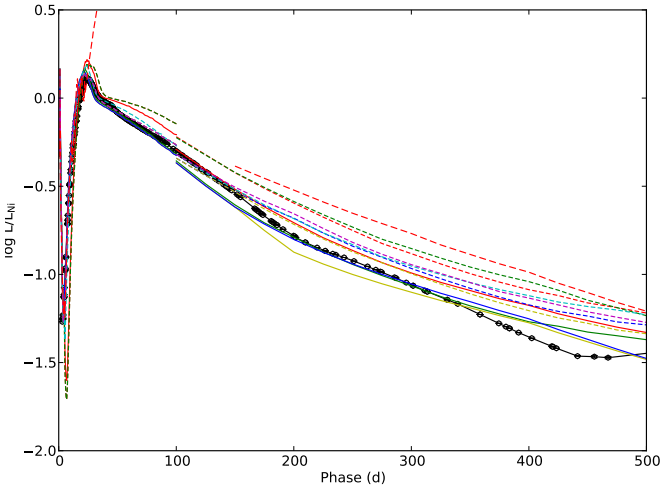

Fig. 22. U to 4.5 μm pseudo-bolometric lightcurves for the 12A (red solid line), 12B (green solid line), 12C (blue solid line), 13A (red short-dashed line), 13B (green short-dashed line), 13C (blue short-dashed line), 13D (yellow short-dashed line), 13E (mangenta short-dashed line), 13F (cyan short-dashed line) and 17A (red long-dashed line) J13 models as compared to the observed U to 4.5 μm bolometric lightcurve. The lightcurves shown in this figure and Fig. **??**, 24 and 25 have been normalized to the radioactive decay chain luminosity of 0.075 $M_\odot$ of ^{56}Ni.

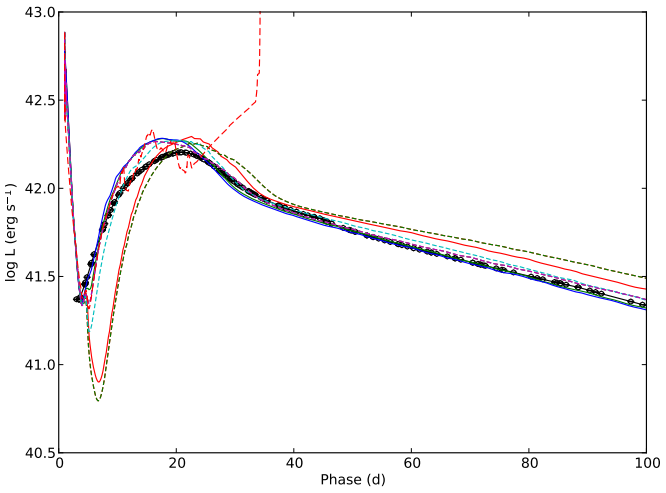

Fig. 23. U to 4.5 μm bolometric lightcurves for the J13 models as compared to the observed U to 4.5 μm bolometric lightcurve for the first 100 days. The lightcurves are displayed as in Fig. 22.

last spectrum. All strong lines arising from other core zones than the Fe/Co zone, as the Mg I] 4571, O I 6300,6364 and Ca II 7291,7323 Å lines have dissappeared or dimished dramatically, which is consistent with a scenario where all the positrons are being trapped locally in the Fe/Co zone.

The effect of molecule cooling on the lightcurves is discussed in Sect. 4.3 and the effect of dust absorption and emission is discussed in Sect. 4.2

Figure 26 shows the fraction of the bolometric luminosity within the *U* to 4.5μm (3300-50000) Å range between 100 and 750 days for the J13 ejecta models.

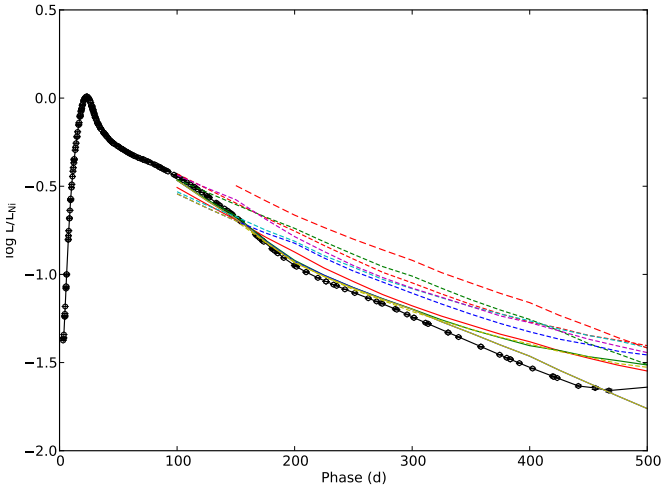

Fig. 24. U to z bolometric lightcurves the J13 models as compared to the observed U to z bolometric lightcurve. The lightcurves are displayed as in Fig. 22.

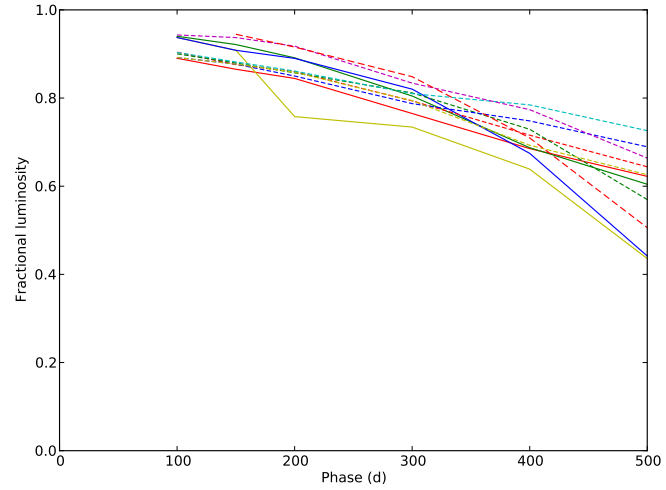

Fig. 26. Fractional U to 4.5 μm bolometric luminosity for the J13 models.

4.2. Dust absorption and emission

As discussed in Sect. 3.3 and seen in Fig. 9 there is a strong increase in the fractional MIR luminosity between ~100 and ~200 days. As also discussed in Sect. 3.3 and seen in Fig. 7 there is a significant increase in the decline rates of the *U* to *K* pseudo-bolometric lightcurve between ~100 and ~200 days, even more pronounced in the *U* to *z* pseudo-bolometric lightcurve (Fig. 24) but less so in the *U* to 4.5 μm pseudo-bolometric lightcurve (Fig. 22). This suggests that some process, re-distributing flux from the optical and NIR to the MIR, is active during this period. One example of such a process is dust formation in the ejecta that would absorb the still quite hot radiation from the SN and re-emit it at a much lower temperature. However, a change of the lines dominating the cooling of the ejecta in some zone could cause a similar effect. As discussed in Sect. 3.3 an increasing excess in the MIR during this period is also seen in SN 1993J but the corresponding increase in the deline rates of the *U* to *K* pseudo-bolometric lightcurve is not seen which makes the interpretation less clear. However, circum stellar medium (CSM)

interaction that would affect the lightcurve in the opposite way could be important for SN 1993J already at this early phase.

Dust is included in the modelling in a simplified way and is represented as a gray opacity in the core (Fe/Co-O/C) zones. The absorbed luminosity is re-emitted as blackbody emission from a homologously expanding surface representing a number of opticaly thick dust clouds. The fractional area of this surface x_{dust} as compared to the area of the core is a free parameter in the modelling and determines the temperature of the emitted blackbody radiation. Note that our treatment of dust absorption and emission is only consistent if the number of dust clouds is large and the filling factor of those is small. At the temperatures expected for dust emission ($\lesssim$2000 K) the luminosity will be increased in the MIR and partly in the NIR and decreased by a factor roughly equal to the total optical depth of the dust in the optical.

Using our simplified dust model we find a value of 0.25 for the optical depth of the dust to match the behaviour of the optical lightcurves (see above). The value of x_{dust} was derived by minimization of the sum of squares of the relative flux differences of model and observed K, 3.6 and 4.5 μm photometry at 200, 300, 400 and 500 days (excluding K when the NIR coverage ends). This gives a value of x_{dust} of 0.01 which corresponds to temperatures of 2000, 1100, 666 and 416 K at 200, 300, 400 and 500 days respectively. However, assuming a large number of dust clouds and a small filling factor it is possible to show from the assumptions made that $\tau = 3/4 x_{dust}$ so this value of x_{dust} does not seem consistent with our assumptions. Furthermore, as seen in Fig. 25 the evolution of the MIR bands is not well reproduced by the optimal model (12C) although the discrepancy is much worse for the same model without dust (12D). The discrepancy in the 4.5 μm magnitudes could possibly be explained by additional flux from the CO fundamental band but the discrepancy in the 3.6 μm band will remain. Clearly the simplified dust model used is not good enough to well explain the MIR evolution and further work is needed to better understand the evolution in these bands. On the other hand, as seen in Fig. 24 the optimal model (12C) gives a good fit to the evolution in the optical, in particular to the increased decline rates between 100 and 200 days, and does improve the discrepancy in the MIR considerably as compared to the same model without dust (12D).

As a further complication there might also be a contribution from heated CSM dust to the MIR emission. Helou et al. (2013) show that such a model could explain the early MIR evolution whereas they fail to reproduce the late evolution. We have not investigated such models but it is possible that a combination of emission from ejecta dust, CSM dust and molecules could well explain the MIR evolution. However, as the observational constraints are limited there is not clear how to disentangle the contributions from these different sources from each other.

4.3. Molecule emission

As discussed in E13 there is an excess in the 4.5 μm band developing during the first hundred days as compared to a blackbody fits to the optical and NIR photometry. As seen in Fig. 10 this excess continues to develop after 100 days and at ~600 days the 4.5 μm band is a factor of ~100 times brighter as compared to such a blackbody fit. Although the interpretation of a blackbody fit to nebular photometry is far from clear we find a similar factor if we compare to synthetic photometry on the J13 model spectra for the models without dust absorption/emission and molecule cooling (Fig. 25). Clearly molecule (CO and SiO), dust or some other source of emission is needed to explain this discrepance. However, even if we exclude other explanations it is not easy to disentangle between a molecule and dust origin.

As discussed in Sect. 3.4.9 we do detect CO first overtone emission at ~200 days and probably at ~100 days. This implies at least some contribution from CO fundamental band emission to the 4.5 μm flux. Knowledge of the fundamental to overtone band flux ratio would make an estimate of the contribution from fundamental band emission to the 4.5 μm flux possible. For SN 1987A this ratio was ~1 at 100 days, a few at 200 days but increased dramatically to ~100 towards 500 days. As discussed in Sect. 3.4.9 we can set upper limits on the fundamental to overtone band flux ratio of ~20 and ~30 at ~100 and ~200 days respectively so assuming the same flux ratios as for SN 1987A would suggest a minor contribution to the 4.5 μm flux from fundamental band emission at these epochs. However, such an assumption does not have a particulary good support as the mass, density and composition of the ejecta is quite different for a Type IIb SNe as compared to SN 1987A. On the other hand, as synthetic photometry on the J13 model spectra for the models with full molecule cooling give to bright 4.5 μm magnitudes (Fig. 25) we know that the amount of molecule cooling has to be intermediate.

Molecule cooling is included in the modelling in a simplified was and is represented as the fraction of the deposited radioactive decay energy emitted as molecule (CO and SiO) emission in the O/C and O/Si/S zones. This energy is then emitted as CO and SiO fundamental and first overtone band emission represented as square line profiles with the typical widths of these emission bands. The ratios of the fundamental and first overtone band emission are assumed to be the same as for SN 1987A. We have used two configurations, one where there the fraction of deposited radioactive decay energy emitted as molecule emission have been set to one and one where this fraction have been set to zero.

4.4. Time dependent effects and the late-time bolometric lightcurve

In this section we will discuss (briefly) time dependent effects and the late-time bolometric lightcurve based on the modelling by Claes.

4.5. Modeling of the bolometric lightcurve day 0-100

In this section we use the HDE code to construct a large model grid allowing us to find the parameters giving the best fit to the bolometric lightcurve and the photospheric velocities in a more quantitative way than in B12. This allows us to refine the disussion of the sensitivity of the derived quantities to errors in the observed quantites initiated in E13. It also allows us to fit the bolometric lightcurves of SNe 1993 and 2008ax using the same model grid and refine the discussion of the nature of their progenitors initiated in E13. We restrict the model grid to consist of bare helium core models without a hydrogen envelope and as in B12 the diffusion phase and the early tail lightcurve and the photospheric velocities are used to determine the parameters of the helium core. We also make the assumption, justified for Type IIb SNe, that the helium core is not affected by mass loss. The thin hydrogen rich envelope only affects the bolometric lightcurve in the cooling phase and the paremeters of this envelope has to be modelled separately. The details of the HDE code and all the caveats related to this type of modelling are discussed in Appendix A.

The parameters varied are the mass of helium core M_{He}, the explosion energy E, the mass of ejected ^{56}Ni M_{Ni} and the distribution of it. The mass fraction of the ^{56}Ni was assumed to be a linearly declining function of mass becoming zero at some fraction of the total mass Mix_{Ni}. The parameter space spanned was M_{He}=2.5-6.5 $M_\odot$, E=0.5-2.0×10^{51} erg, M_{Ni}=0.02-0.2 and Mix_{Ni}=0.5-1.0 using a 10×10×10×10 grid. We have found this resolution to be sufficient to safely interpolate intermediate values. The fitting is done by minimizing the square of the relative residuals giving equal weight to the diffusion phase lightcurve (5-40 days), the tail lightcurve (40-100 days) and the early photospheric velocity evolution (5-40 days). As stellar models we have used solar metallicity STARS models (Stancliffe & Eldridge 2009), removing the hydrogen envelope and re-calculating the density profile using the constraints from hydrostatic and thermal equilibrium as described in B12 (! Fix this !). As the HDE code does not include a network of nuclear reactions the explosive nucleosynthesis as a function of mass and explosion energy, except for the syntesized ^{56}Ni (see above), have been adopted from Woosley & Heger (2007) (! Fix this !) and linearly interpolated.

Fig. 27 shows the model and observed lightcurve and photospheric velocity evolution for the optimal models of SNe 2011dh, 2008ax and 1993J as well as contour plots of the error in the fit as a function of helium core mass and energy. Table 3 shows the helium core mass, explosion energy, mass of ejected ^{56}Ni and the distribution of it for the optimal models and the corresponding errors. The errors were calculated as the square root of the sum of the squared errors resulting from the errors in distance and extinction and a systematic error in the photospheric velocities. The derived parameters for SN 2011dh are in good agreement with the results in B12. The helium core mass and explosion energy derived for SNe 1993J and 2008ax are similar to what is derived for SN 2011dh wheras the mass of ejected ^{56}Ni differs significantly. The ^{56}Ni is distributed far out in the ejecta for all three SNe. We note that the velocity evolution of SN 2008ax is not well fitted which could be explained by a worse correspondance between the absorption miniumum of Fe II 5169 Å and the photosphere as compared to SNe 2011dh and 1993J. The countor plots show that, as expected and discussed in E13, there is as a strong degenerecy in helium core mass and explosion energy if the fitting is done using the bolometric lightcurve alone. As seen in the constraint from the photospheric velocity evolution decrease this degeneracy significantly and the fit becomes quite robust. This means however that we expect the results to be quite sensitive to errors in the photospheric velocities.

Fig. 28 shows the sensitivity of the derived quantities to errors in the distance, extinction and a systemtic error in the photospheric velocity. For the helium core mass and explosion energy the dependence on the distance and extinction is weak although a higher extinction or larger distance tends to lower the helium core mass. The dependence on the photospheric velocity on the other hand is quite strong. For the mass of ejected ^{56}Ni the sensitivity on the distance and extinction is strong whereas the dependence on the photospheric velocity is weak. The dependencies of the derived quantities on the distance and extinction are in agreement with the qualitative discussion in E13 but our model grid now makes it possible to quantify these as well as the dependencies on the photospheric velocity. In general we see that an error in the distance and extinction mainly corresponds to an error in the mass of ejected ^{56}Ni whereas an error in the photospheric velocity mainly corresponds to an error in the helium core mass and explosion energy. In Fig 28 we also show the dependencies as expected from approximate considerations. As discussed in E13 we expect the mass of ejected ^{56}Ni to be proportional to the distance and, if we assume that the SED is peaking near the V band and the change in extinction is reasonably small, to be proportional to $10^{A_V/2.5}$. As the diffusion time depends on the ejecta mass and explosion energy as E/M^3 and the velocity squared as E/M we expect the ejecta mass to be proportional to the velocity and the energy to be proportional to the velocity cubed. As seen in the figure these approximate scalings are well followed by the model.

To calculate the error bars for the derived quantities in Table 3 we have assumed a systematic error in the photosperic velocity of 15 percent. As discussed in E13 the photospheric radius as measured from the absorption minimum of the Fe II 5169 Å line could be overestimated by as much as ∼30 percent for SN 2011dh if we treat the thermalization radius as estimated from blackbody fits to the photometry as a lower limit. Such an error would ruin our lower error bars on the mass and explosion energy wheras the upper error bars would remain unchanged. However, such a ∼30 percent overestimate corresponds to an dilution factor (ratio between thermalization and photospheric radii) of 1.0 which is not particularly likely. Actually, the average observed dilution factor between 5 and 40 days of ∼0.75 equals the average model dilution factor (Sect. 5.1) between 5 and 25 days (where the thermalization radius disappears in the modelling). Although this argument is only indicative and the observed dilution factor is not known with better accuray than the distance we find the 15 percent error used in the calculation reasonable.

We find a similar good agreement between average observed and model dilution factors for SN 1993J but as discussed in (Sect. 5.1) for SN 2008ax the average observed and model dilution factors is ∼0.5 and ∼0.80 respectively and the observed blackbody temperature is also much higher than the model thermalization thermperature. This is a clear indication that the adopted extinction is overestimated although the comparison has a number of caveats and other explanations are possible. As discussed above the derived mass and explosion energy are weakly dependent on the adopted extinction and the significant uncertainly in this quantity for SN 2008ax is included in the calculation of the error bars in Table 3. To get a better correspondance between observed and model dilution factors and temperatures the extinction for SN 2008ax would need to be revised towards the lower error limit which would correspond to an increase of the derived mass to ∼3.5 $M_\odot$ (!verify this!). The derived mass of the ejected ^{56}Ni on the other hand would be very sensitive to such a revision and reduced with a factor of ∼2 (!verify this!) which, as discussed in E13, makes some sense as we find the other explosion parameters (helium core mass and explosion energy) to be similar to those of SNe 2011dh.

4.6. Modeling of the bolometric lightcurve day 0-300

In this section we extend the temporal coverage of the model grid described in Sect. 4.5 to 300 days (which is the period for which we have full U to 4.5 μm coverage) and make a fit of the observed U to 4.5 μm pseudo-bolometric lightcurve of SN 2011dh to the model grid in a way similar to what was done in Sect. 4.5. The method used is to calculate the bolometric lightcurve after 100 days using the HDE code assuming homologous expansion and instant emission of the energy deposited by the radioactive decay chains. However, to compare with the pseudo-bolometric lightcurve after 100 days we also include a correction for the flux

Table 3. Helum core mass, explosion energy, mass of the ejected ^{56}Ni and the distribution of it for the optimal models of SNe 2011dh, 1993J and 2008ax.

SN	E (10^{51} erg)	M_{He} ($M_\odot$)	M_{Ni} ($M_\odot$)	Mix_{Ni}
2011dh	0.60 (+0.40,-0.24)	3.50 (+0.62,-0.52)	0.062 (+0.028,-0.006)	1.00 (+0.00,-0.00)
2008ax	0.60 (+0.62,-0.20)	3.12 (+0.67,-0.40)	0.162 (+0.095,-0.091)	0.95 (+0.00,-0.09)
1993J	0.60 (+0.50,-0.20)	3.38 (+0.52,-0.41)	0.100 (+0.028,-0.028)	1.00 (+0.00,-0.23)

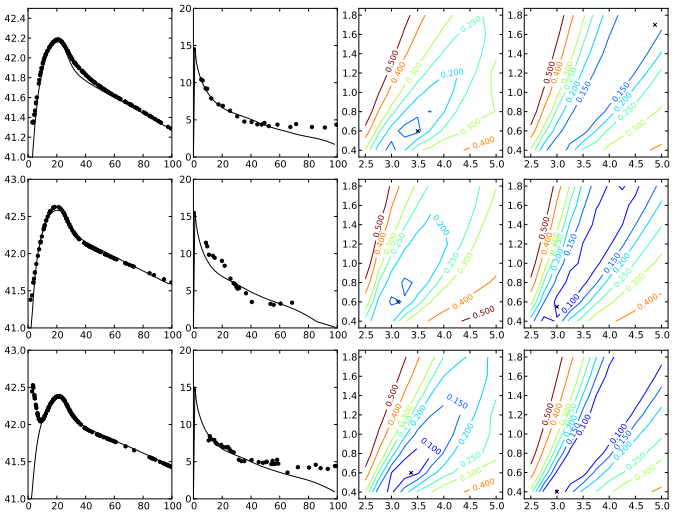

Fig. 27. Bolometric lightcurve (right panels) and photospheric velocity evolution (middle left panels) for the optimal models as compared to the observed U to K pseudo-bolometric lightcurves and the velocity evolution of the absorption minimum of Fe II 5169 Å for SNe 2011dh (top panels), 2008ax (middle panels) and 1993J (bottom panels). In the middle right and right panels we show contour plots of the error in the fits as a function of mass and explosion energy for the case where the photospheric velocities were used and not used respectively.

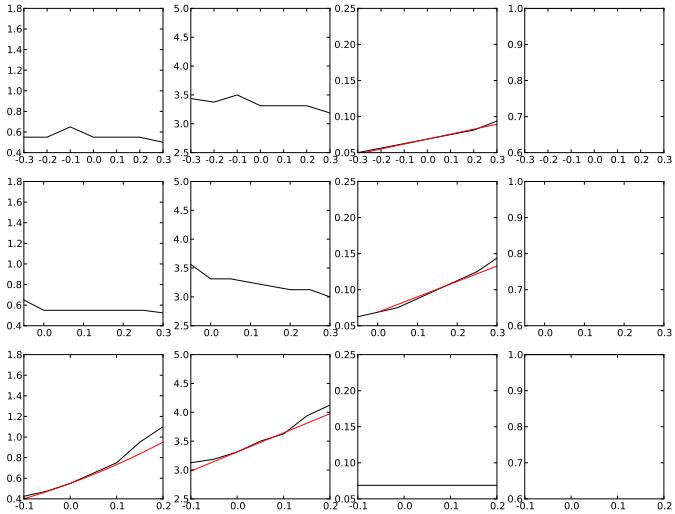

Fig. 28. Sensitivity of the derived explosion energy (left panels), helium core mass (middle left panels), mass of ejected ^{56}Ni (middle right panels) and the distribution of it (right panels) on an error in the distance (upper panels), extinction (middle panels) and photospheric velocities (lower panels).

within the U to 4.5 μm wavelength range determined with the steady-state NLTE code. Fig. 29 shows the bolometric lightcurve for the optimal bare helium core model for SN 2011dh as compared to the observed U to 4.5 μm pseudo-bolometric lightcurve, calculated as described and multiplied with the fraction of bolometric flux within the U to 4.5 μm wavelength range for the optimal NLTE model after 100 days.

Although Fig. 29 is quite convincing a quantative fit as in Sect. 4.5 is needed to determine the error sensitivity and degeneracy of the solution. In anology with the procedure described in Sect. 4.5 the fitting is done by minimizing the square of the relative residuals giving equal weight to the diffusion phase lightcurve (5-40 days), the early tail lightcurve (40-100 days), the late tail lightcurve (100-300 days) and the early photospheric velocity evolution (5-40 days). This weighting scheme give less weight to the photospheric velocities but this is also motivated as we have additional information about the lightcurve.

The correction for the flux within the U to 4.5 μm wavelength range was determined by evolving a strongly restricted set of the ejecta models with the steady-state NLTE modelling. In most of the parameter space spanned this correction did not vary much and the number of ejecta models were chosen as small as possible to get a reasonable precision (~10 percent) using linear interpolations. The further restrict the number of ejecta models we excluded those for which the average bolometric luminosity was more than 25 percent below the average observed U to 4.5 μm luminosity using the lower error bars for the distance and extinction as we know these would never make a good fit.

The method has its limitations and all the free parameters of the steady-state NLTE modelling which are not possible to map from the hydrodynamical modelling, as the degree of macroscopic mixing, the fraction of the energy going into molecule cooling in the O/C and O/Si zones and the amount of dust, have to be assigned some values. Here we have chosen to give these parameters the same values as for our optimal steady-state NLTE model (Sect. 4.1). On the other hand, as seen in Fig. 26 the fractional flux within U to 4.5 μm does not vary much between the J13 ejecta models during the first 300 days and as the optical depth to the γ-rays (and thus the deposited energy) depends on the ejecta mass as M^2/E we don't expect the derived helium core mass to be very sensitive to changes in this fraction.

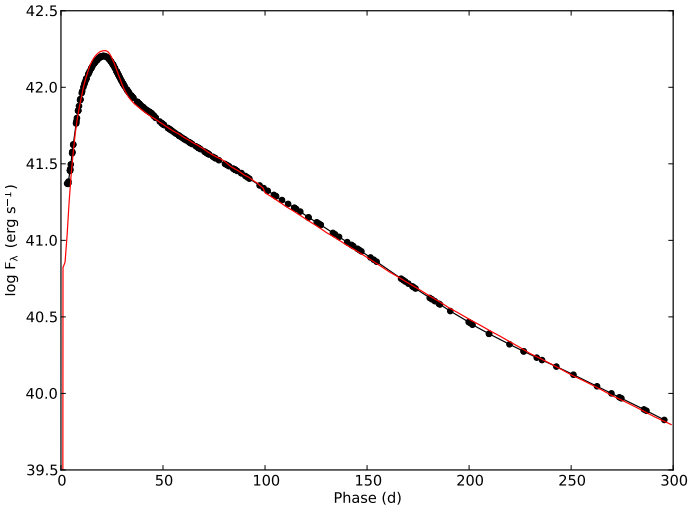

Fig. 29. Bolometric lightcurve for the optimal bare helium core model for SN 2011dh (red solid line) as compared to the observed U to 4.5 μm pseudo-bolometric lightcurve for the first 300 days (black dots and solid line). After 100 days the optimal bare helium core model flux have been multplied with the fraction of bolometric flux within the U to 4.5 μm wavelength range for the optimal NLTE model.

5. Discussion

5.1. Physical interpretation of photometric and spectral evolution

In this section we discuss how the photometric and spectroscopic evolution could be understood given our optimal model, a 3.5 $M_\odot$ helium core with a thin 270 $R_\odot$ envelope exploded with an energy of $0.6{\times}10^{51}$ erg, ejecting 0.075 $M_\odot$ of ^{56}Ni. When the shock reaches the hydrogen rich envelope at $\sim10^2$ seconds the explosion energy is roughly equi-partioned between kinetic and thermal energy and the shock speed is $\sim2{\times}10^4$ km s^{-1}. In the nearly constant density envelope the shock is decelerated to $\sim1{\times}10^4$ km s^{-1} and when the radiation breaks out from the shock at $\sim10^4$ seconds almost all of the thermal energy deposited in the helium core has been cold away by expansion. About on tenth of the explosion energy is deposited in the hydrogen envelope but even here equi-partition is not reached and at shock breakout only a small fraction of the explosion energy is in the form of thermal energy. Fig. 30 shows the density and temperature profiles at shock breakout. Because of the decelaration of the shock the hydrogen envelope has been strongly compressed and the temperature is high. In the three days that follows the hydrogen envelope will accelerate and expand and the temperature and luminoisity at the photosphere, which are initially very high, will decrease rapidly because of expansion cooling and the short diffusion time for the radiation. This is the cooling phase seen in the early photometry published in Arcavi et al. (2011) and Tsvetkov et al. (2012).

The cooling phase ends at ~3 days when our observations begins and is followed by the diffusion phase which corresponds to the diffusion of the thermal energy deposited in the ejecta by the radioactive decay chain of ^{56}Ni and was discussed in some detail in E13 as understood by approximate models (Arnett 1982; Imshennik & Popov 1992). In our optimal model of SN 2011dh the photosphere reaches the helium core at 4.5 days, after which the position of the photosphere is determined by the ionization front of helium slowly moving inwards in mass coordinates but outwards in radial coordinates. Defining the thermalization radius as $\sqrt{3\tau_{abs}\tau_{tot}} = 2/3$ (Ensman & Burrows 1992) this is located near the outer edge of the ionization front of helium and follows the evolution of this until ~25 days when helium recombines and the thermalization surface cease to exist. In Fig. 31 we show the dilution factor (ration of thermalization and photospheric radii) for the optimal bare helium core models for SNe 2011dh, 1993J and 2008ax compared to the observed dilution factor as estimated from blackbody fits to the $VIJHK$ photometry and the measured absorption minimum of the Fe II 5169 Å line. We also show the thermalization temperature compared to the observed temperature as estimated from blackbody fits to the $VIJHK$ photometry.

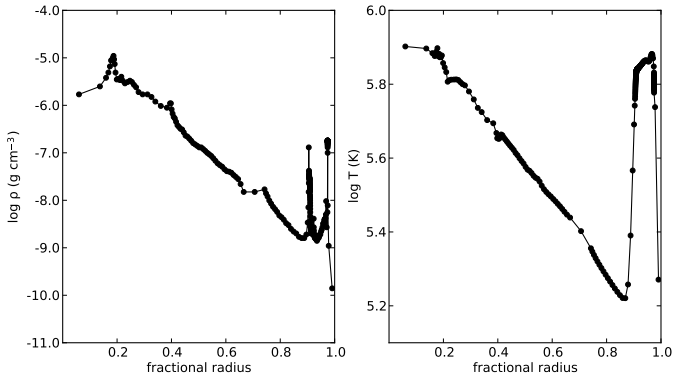

Fig. 30. Density (left panel) and temperature (right panel) profiles of the optimal model for SN 2011dh at shock breakout.

Before the temperature peak the observed temperature of SNe 2011dh and 1993J is lower and the observed dilution factor higher than in the model, possibly because of the presence of the hydrogen envelope, but after this the agreement is good. The model temperatures and dilution factors for all SNe are fairly constant at ~9000 K and ~0.8 respectively. The observed temperature of SN 2008ax on the other hand is much higher and the observed dilution factor much lower. In the modelling the thermalization temperature is mainly determined by the ionization temperature of helium and to reach a temperature above 15000 K at the center of the ionization front in a pure helium envelope requires a density higher than 10^{-9} g cm^{-1} which is a factor of 100 above the canonical 10^{-11} g cm^{-1}. Although there is a number of caveats, as the variation of the thermalization radius and thus the temperature with wavelength (Dessart & Hillier 2005) and the relation between this temperature and a blackbody fit to the $VIJHK$ photometry, we find the discrepancey intriguing. One obvious explanation is that the extinction adopted for SN 2008ax is overestimated but other explanations as differences in density and composition might be possible as well.

5.2. The nature of the progenitor star

In M11, B12, E13, J13 and this paper we have investigated the nature of the progenitor star using a number of different and, at least partially, independent methods. In M11 we analysed direct observations of the star by comparison of the observed magnitudes to predictions from stellar athmosphere and evolutionary models. The best match was found to be a yellow supergiant with an initial mass of 13±3 $M_\odot$ and a radius of ~270 $R_\odot$. In E13 we presented observations of the disappearence of this star thus confirming that it was the progenitor of SN 2011dh.

In B12 we presented hydrodynamical modeling, which given the refinements in E13, shows that a star with a helium core of

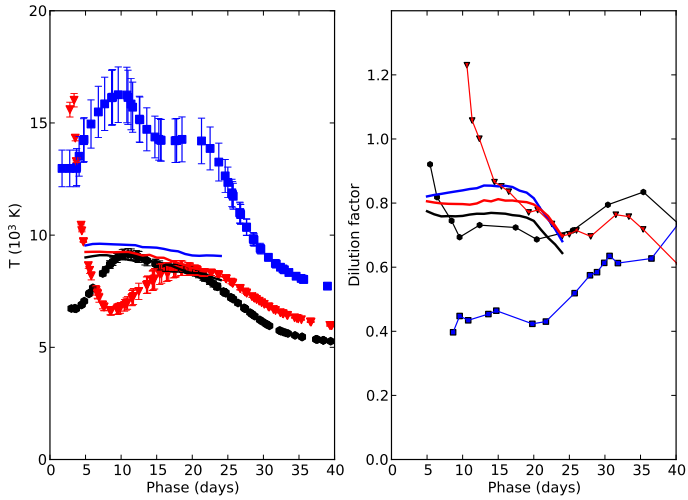

Fig. 31. Left panel: Observed blackbody temperature for SNe 2011dh (black dots), 1993J (red triangles) and 2008ax (blue squares) compared to the thermalization temperature as estimated from the hydrodynamical modelling (solid lines). Right panel: Observed dilution factor for SN 2011dh (black dots), 1993J (red trangles) and 2008ax (blue squares) compared to the dilution factor as estimated from the hydrodynamical modelling (solid lines).

3-4 $M_\odot$ and a thin (0.1 $M_\odot$) and extended (200-300 $R_\odot$) envelope, exploded with an energy of 0.6-1.0×10^{51} erg and ejecting 0.05-0.10 $M_\odot$ of ^{56}Ni mixed out to a velocity of ∼9000 km s^{-1} well reproduce the observed bolometric lightcurve for the first 100 days. In this paper we arrive at similar best fit values using hydrodynamical modeling to scan a large volume of parameter space where we have also extended the temporal coverage to 300 days by the use of a correction for the flux within the observed wavelength range determined with steady-state NLTE modelling.

In J13 we presented steady-state NLTE modelling of nebular spectra showing that a star with an initial mass of ∼12 $M_\odot$ best reproduce the observed spectral evolution with particular focus on the [O I] 6300/6364 lines which are very sensitive to the initial mass of the star. In this paper we find the optimal model from J13 to give a reasonable fit to the observed U to 4.5 μm and U to z pseudo-bolometric lightcurves between ∼100 and ∼450 days and to the observed U to K pseudo-bolometric lightcurve until the NIR coverage ends at ∼300 days. After ∼450 days we cannot reproduce the observed evolution of the pseudo-bolometric lightcurves but it is clear from modelling using a time-dependent NLTE code (Kozma & Fransson 1992, 1998a,b) that in this phase freeze-out in the helium zone is important and the assumption of steady-state is no longer valid.

In E13 we estimated a hydrogen mass of 0.01-0.04 $M_\odot$ using a Monte-Carlo atmosphere code in agreement with the 0.024 $M_\odot$ estimated by Arcavi et al. (2011) using a similar but more advanced code that included a NLTE treatment of hydrogen and helium. This hydrogen mass is consistent with the B12 ejecta model and we also find the interface between the helium core and the hydrogen rich envelope to be located at a velocity consistent with this model.

As proposed in E13 and shown in this paper the sensitivity of the mass and explosion energy derived from the hydrodynamical modelling to the errors in distance and extinction is weak and merely effects the derived mass of ejected ^{56}Ni. Although we have not scanned parameter space with the steady-state NLTE code as this would be too computationally intensive a similar conclusion is likely to hold for the initial mass as estimated from nebular spectra with steady-state NLTE code. The fitting procedure for the hydrodymanical modelling used in this paper also allows us to quantify the sensitivity to errors in the photospheric velocities and including errors in all the observables the upper bound on the initial mass is found to be ∼15 $M_\odot$.

In all the results obtained with the different methods are consistent and, even given the caveats of each individual method, it is likely that the progenitor star is of moderate initial mass (10-15 $M_\odot$) and has a thin extended hydrogen rich envelope of which most must have been lost either through stellar winds or interaction with a binary companion. The moderate mass suggests that interaction with a binary is needed as stellar winds of stars in this mass range are not strong enough to expell the hydrogen envelope before core-collapse. As we show in J13 and in this paper, using steady-state NLTE modelling of nebular spectra and hydrodynamical modelling of the bolometric lightcurve, SNe 2008ax and 1993J are likely to be of similar initial mass and have similar explosion energy as SN 2011dh although the mass of the ejected ^{56}Ni may differ significantly depending on the distance and extinction adopted. In particular the upper bound on the initial mass for all three SNe is found to be ∼15 $M_\odot$. By the same reason as discussed above this suggests that interaction with a binary have taken place and removed most of the hydrogen envelope of their progenitor stars. In the case of SN 1993J this conclusion is supported by direct observations of the binary companion (Maund et al. 2004). Observations that could detect or set useful constraints on the presence of a companion star for SN 2011dh are schedulded for Cycle 21 at HST whereas similar observations for SN 2008ax would not be feasible because of the larger distance. Clearly there is growing evidence that the main production channel for Type IIb SNe are stars stripped on their hydrogen envelope by interaction with a binary companion. Modelling of the nebular spectra and hydrodynamical modelling of the bolometric lightcurves for a larger sample of Type IIb SNe could provide further evidence for this hypothesis.

6. Conclusions

We present nealy two years of optical and NIR photometric and spectroscopic observations for the Type IIb SN 2011dh. Together with SWIFT UV and Spitzer MIR data we build a UV to MIR pseudo-bolometrci lightcurve covering ∼700 days, although the photometric coverage ends at ∼100 days in UV and at ∼350 days in NIR. The spectral coverage ends at ∼200 days in NIR and ∼450 days in the optical.

We have used a steady-state NLTE code (Jerkstrand et al. 2011, 2012, 2013) to find a 12 $M_\odot$ ejecta model that reproduce the U to 4.5 μm and U to z pseudo-bolometric lightcurves until ∼450 days and the U to K pseudo-bolometric lightcurve until ∼300 days (when the NIR coverage ends) reasonably well. However, we are unable to reproduce the evolution after ∼450 days when a considerable flattening is seen in all lightcurves. Modelling with a time-dependent NLTE code (Kozma & Fransson 1992, 1998a,b) show that in this late phase freeze-out in the helium zone becomes important and therefore the assumption of steady-state is no longer valid.

The suggestion by Shivvers et al. (2013) that the SN has entered a phase powered by the positrons emitted in the ^{56}Co decay after 300-350 days is found to be roughly correct in the sense that the positron deposition dominates the γ-ray deposition after ∼400 days in our optimal model. However, the emitted flux is probably dominated by recombinations in the helium zone

and/or other time-dependent processes so neither the luminosity nor the decline rates are likely to be determined by the positrons emitted in the ^{56}Co decay.

We have used the hydrodynamical HDE code to build a model grid for the early (3-100 days) lightcurve spanning a large volume of parameter space. This allows a more quantitatve fitting procedure than was used in B12 as well as a consistent modelling of SNe 2011dh, 1993J and 2008ax taking into account the significant errors in distance and extinction. The results for SN 2011dh are in good agreement with those found in B12. For SNe 1993J and 2008ax we find values of the mass and explosion energy similar to those of SN 2011dh whereas the mass of ^{56}Ni depends sensitively on the adopted distance and extinction. The mass and explosion energy on the other hand are unsensitive to changes in the distance and extinction which is an important quality of the modelling.

We have also constructed an extended model grid with temporal coverage up to 300 days by assuming instant emission of the energy deposited by the radioactive decay chains after 100 days. To compare with the observed U to 4.5 μm pseudo-bolometric lightcurve we have determined the fractional flux within this wavelength range with the steady-state NLTE code. This allows us to combine the power of the hydrodynamical and steady-state NLTE modelling and the use of a quantiative fitting procedure. Applying this to the observed 3-300 days U to 4.5 μm pseudo-bolometric lightcurve of SN 2011dh we find best fit values for the mass, explosion energy, mass of ejected ^{56}Ni and the distribution of it in good agreement with those based on the 3-100 days bolometric lightcurve.

We find an excess in the MIR and NIR as compared to steady-state NLTE model photometry developing between ∼200 and ∼300 days, during which an increase in the optical and NIR tail decline rates is also observed. This behaviour could be reproduced by the steady-state NLTE modelling if a modest amount of dust ($\tau = 0.2$) is being continiously formed in the ejecta during this period, although the photomeric evolution in the MIR is not well reproduced after ∼400 days.

However, as discussed in E13 an excess is developing in the 4.5 μm already during the first 100 days. This is unlikely to be caused by dust forming in the ejcta but CO fundamental band emission or a thermal dust echo as proposed by Helou et al. (2013) are possible explanations. We detect CO first overtone band emission in NIR spectroscopy at ∼100 and ∼200 days so there is certainly a contribution to the observed 4.5 μm band flux from CO fundamental band emission at these epochs and probably at earlier and later epochs as well.

In general the physical explanation for the photometric evolution in the MIR bands could be quite complex and might involve components from CO emission, SiO emission, ejecta and circumstellar dust emission for which, at the best, only a simple and approximate treatment is included in the steady-state NLTE modelling.

7. Acknowledgements

Appendix A: Hydrodynamical modelling

For the hydrodynamical modelling done in this paper we use the HDE code, similar in most aspects to the code used in B12 implementing the method described in Falk & Arnett (1977) and Bersten et al. (2011). The hydrodynamical conservation equations for mass, momentum and energy (Falk & Arnett 1977, eqs. 1-4) are solved by a finite difference scheme similar to the one described by Falk & Arnett (1977, eqs A1-A12) assuming that the radiative flux is given by the diffusion approximation (Falk & Arnett 1977, eq. 5). This is motivated in the optically thick regime but not in the optically thin regime where the radiation field is decoupled from the matter. In the optically thin regime we use a flux limiter following the prescription given by Bersten et al. (2011), being essentially a transformation of the radiation field from the optically thick to the optically thin limit. To handle strong velocity gradients (shocks) we use an artificial viscosity following the prescription by Von Neumann & Richtmyer (1950). The opacity is calculated from the OPAL opacity tables (Iglesias & Rogers 1996) complemented with the low temperature opacities given by Alexander & Ferguson (1994). These opacity tables are calculated for a non-expanding medium and therefore the bound-bound opacity, which is strongly dependent on the velocity field, is not applicable to SNe. To handle this we use, as discussed in Bersten et al. (2011), a minimum value of the opacity called opacity floor. The value of this floor is set to 0.01 cm^2 gram^{-1} in the hydrogen envelope and 0.025 cm^2 gram^{-1} in the helium core following B12 who calibrated these values by comparison to the STELLA hydrodynamical code (Blinnikov et al. 1998). The electron density needed in the equation of state is calculated by solving the Saha equation using the same atomic data as in Jerkstrand et al. (2011, 2012). The transfer of the gamma-rays and positrons emitted in the decay chain of ^{56}Ni is calculated with a Monte-Carlo method using the same gray opacities, luminosities and decay times as in Jerkstrand et al. (2011, 2012) and the heating rate then fed into the energy equation. The code may also be run in homolgous mode where the dynamics have been switched off and the energy equation is solved given the constraint of homologous expansion.

The momentum equation was written in explicit finite difference form as

$$\frac{\Delta v_k^n}{\Delta t^n} = -4\pi (r_k^n)^2 \frac{(\Delta P_k^n + \Delta Q_k^n)}{\Delta m_k} - \frac{G m_k}{(r_k^n)^2} \tag{A.1}$$

where

$$\begin{aligned} \Delta v_k^n &= v_k^{n+1/2} - v_k^{n-1/2} \\ \Delta P_k^n &= P_{k-1/2}^n - P_{k+1/2}^n \\ \Delta Q_k^n &= Q_{k+1/2}^n - Q_{k-1/2}^n \end{aligned} \tag{A.2}$$

and solved for $v_k^{n+1/2}$. The energy equation was written in implicit finite difference form as

$$\frac{\Delta E_{k+1/2}^{n+1/2}}{\Delta t^{n+1/2}} = \epsilon_{k+1/2}^{n+1/2} - (P_{k+1/2}^{n+1/2} + Q_{k+1/2}^{n+1/2}) \frac{\Delta V_{k+1/2}^{n+1/2}}{\Delta t^{n+1/2}} - \frac{\Delta L_{k+1/2}^{n+\theta}}{\Delta m_{k+1/2}} \tag{A.3}$$

where

$$\begin{aligned} \Delta E_{k+1/2}^{n+1/2} &= E_{k+1/2}^{n+1} - E_{k+1/2}^n \\ \Delta V_{k+1/2}^{n+1/2} &= V_{k+1/2}^{n+1} - V_{k+1/2}^n \\ \Delta L_{k+1/2}^{n+\theta} &= \theta (L_{k+1}^{n+1} - L_k^{n+1}) + (1-\theta)(L_{k+1}^n - L_k^n) \\ \epsilon_{k+1/2}^{n+1/2} &= (\epsilon_{k+1/2}^{n+1} + \epsilon_{k+1/2}^n)/2 \\ P_{k+1/2}^{n+1/2} &= (P_{k+1/2}^{n+1} + P_{k+1/2}^n)/2 \\ Q_{k+1/2}^{n+1/2} &= (Q_{k+1/2}^{n+1} + Q_{k+1/2}^n)/2 \end{aligned} \tag{A.4}$$

and solved for $T^{n+1}_{k-1/2}$, $T^{n+1}_{k+1/2}$ and $T^{n+1}_{k+3/2}$. This was achived by defining the quantity

$$D^{n+1/2}_{k+1/12} = \Delta E^{n+1/2}_{k+1/2} + (P^{n+1/2}_{k+1/2} + Q^{n+1/2}_{k+1/2})\Delta V^{n+1/2}_{k+1/2} + \Delta L^{n+\theta}_{k+1/2}\frac{\Delta t^{n+1/2}}{\Delta m_{k+1/2}} \tag{A.5}$$

and finding the zero of this function by iteratively solving

$$\frac{\partial D^{n+1/2}_{k+1/2}}{\partial T^{n+1}_{k-1/2}}\delta T^{n+1}_{k-1/2} + \frac{\partial D^{n+1/2}_{k+1/2}}{\partial T^{n+1}_{k+1/2}}\delta T^{n+1}_{k+1/2} + \frac{\partial D^{n+1/2}_{k+1/2}}{\partial T^{n+1}_{k+3/2}}\delta T^{n+1}_{k+3/2} = D^{n+1/2}_{k+1/2} \tag{A.6}$$

for the temperature corrections $\delta T^{n+1}_{k-1/2}$, $\delta T^{n+1}_{k+1/2}$ and $\delta T^{n+1}_{k+3/2}$. The coefficients of this equation system constitutes a tridiagonal matrix which could be inverted by the use of standard methods.

References

Alexander, D. R. & Ferguson, J. W. 1994, ApJ, 437, 879
Arcavi, I., Gal-Yam, A., Yaron, O., et al. 2011, ApJ, 742, L18
Arnett, W. D. 1982, ApJ, 253, 785
Benvenuto, O. G., Bersten, M. C., & Nomoto, K. 2013, ApJ, 762, 74
Bersten, M. C., Benvenuto, O., & Hamuy, M. 2011, ApJ, 729, 61
Bersten, M. C., Benvenuto, O. G., Nomoto, K., et al. 2012, ApJ, 757, 31
Blinnikov, S. I., Eastman, R., Bartunov, O. S., Popolitov, V. A., & Woosley, S. E. 1998, ApJ, 496, 454
Chugai, N. N. 1994, ApJ, 428, L17
Dessart, L. & Hillier, D. J. 2005, A&A, 439, 671
Ensman, L. & Burrows, A. 1992, ApJ, 393, 742
Ergon, M., Sollerman, J., Fraser, M., et al. 2013, ArXiv e-prints
Falk, S. W. & Arnett, W. D. 1977, ApJS, 33, 515
Griga, T., Marulla, A., Grenier, A., et al. 2011, Central Bureau Electronic Telegrams, 2736, 1
Helou, G., Kasliwal, M. M., Ofek, E. O., et al. 2013, ArXiv e-prints
Iglesias, C. A. & Rogers, F. J. 1996, ApJ, 464, 943
Imshennik, V. S. & Popov, D. V. 1992, AZh, 69, 497
Jerkstrand, A., Ergon, M., Smartt, S., & Fransson, C. 2013, In preparation
Jerkstrand, A., Fransson, C., & Kozma, C. 2011, A&A, 530, A45
Jerkstrand, A., Fransson, C., Maguire, K., et al. 2012, A&A, 546, A28
Kozma, C. & Fransson, C. 1992, ApJ, 390, 602
Kozma, C. & Fransson, C. 1998a, ApJ, 496, 946
Kozma, C. & Fransson, C. 1998b, ApJ, 497, 431
Matthews, K., Neugebauer, G., Armus, L., & Soifer, B. T. 2002, AJ, 123, 753
Maund, J. R., Fraser, M., Ergon, M., et al. 2011, ApJ, 739, L37
Maund, J. R., Smartt, S. J., Kudritzki, R. P., Podsiadlowski, P., & Gilmore, G. F. 2004, Nature, 427, 129
Maurer, I., Mazzali, P. A., Taubenberger, S., & Hachinger, S. 2010, MNRAS, 409, 1441
Milisavljevic, D. & Fesen, R. 2010, in Bulletin of the American Astronomical Society, Vol. 42, American Astronomical Society Meeting Abstracts #215, 454.05
Podsiadlowski, P., Hsu, J. J. L., Joss, P. C., & Ross, R. R. 1993, Nature, 364, 509
Sahu, D. K., Anupama, G. C., & Chakradhari, N. K. 2013, MNRAS, 433, 2
Shivvers, I., Mazzali, P., Silverman, J. M., et al. 2013, ArXiv e-prints
Stancliffe, R. J. & Eldridge, J. J. 2009, MNRAS, 396, 1699
Stathakis, R. A., Dopita, M. A., Cannon, R. D., & Sadler, E. M. 1991, Supernovae, 649
Stritzinger, M., Hamuy, M., Suntzeff, N. B., et al. 2002, AJ, 124, 2100
Taubenberger, S., Navasardyan, H., Maurer, J. I., et al. 2011, MNRAS, 413, 2140
Tsvetkov, D. Y., Volkov, I. M., Sorokina, E., et al. 2012, Peremennye Zvezdy, 32, 6
Valenti, S., Fraser, M., Benetti, S., et al. 2011, MNRAS, 416, 3138
Van Dyk, S. D., Li, W., Cenko, S. B., et al. 2011, ApJ, 741, L28
Van Dyk, S. D., Zheng, W., Clubb, K. I., et al. 2013, ApJ, 772, L32
Von Neumann, J. & Richtmyer, R. D. 1950, Appl. Phys., 21, 232
Woosley, S. E. & Heger, A. 2007, Phys. Rep., 442, 269
Yaron, O. & Gal-Yam, A. 2012, PASP, 124, 668

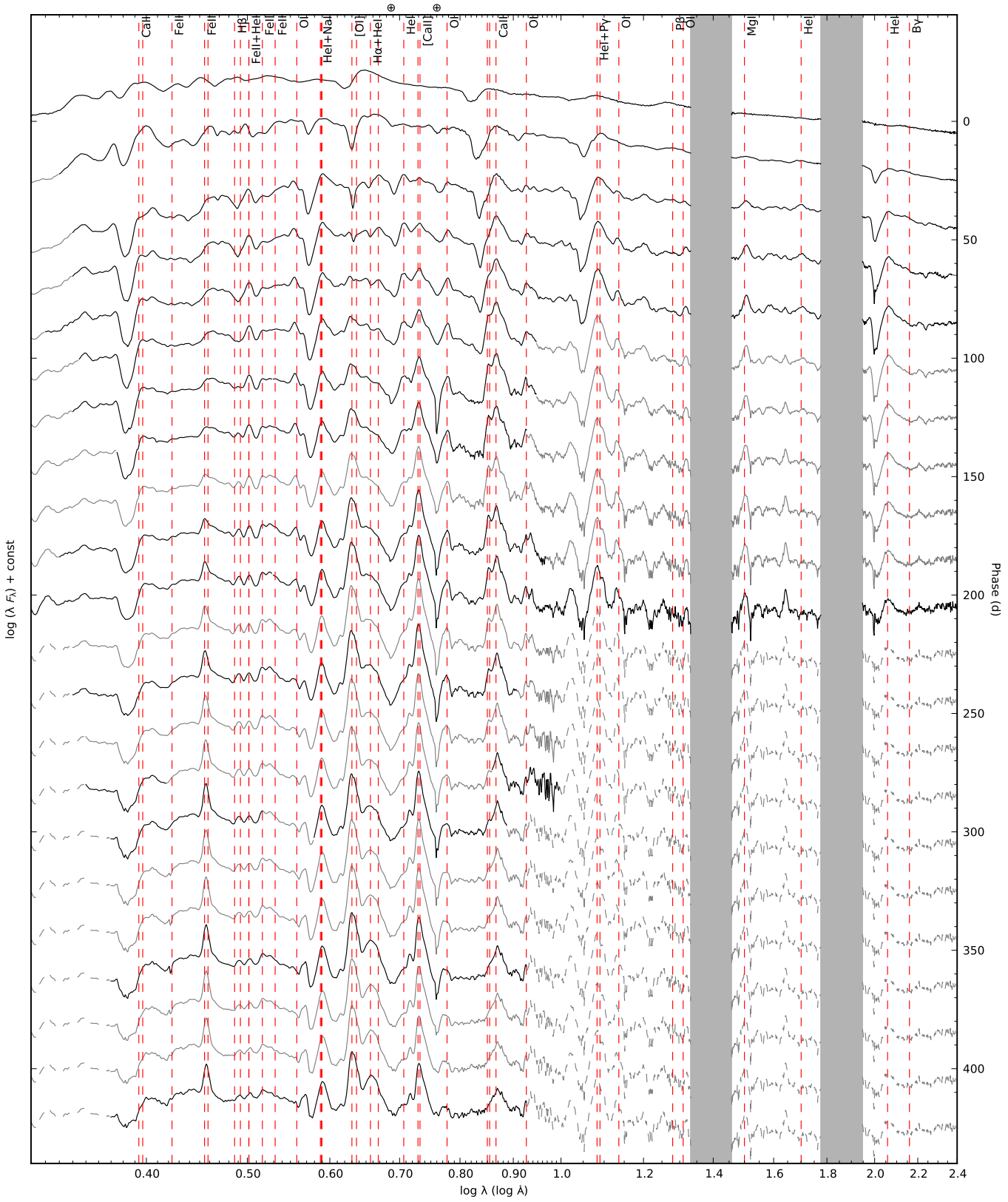

Fig. 2. Optical and NIR (interpolated) spectral evolution for SN 2011dh for days 5−425 with a 20-day sampling. Telluric absorption bands are marked with a ⊕ symbol in the optical and shown as grey regions in the NIR.

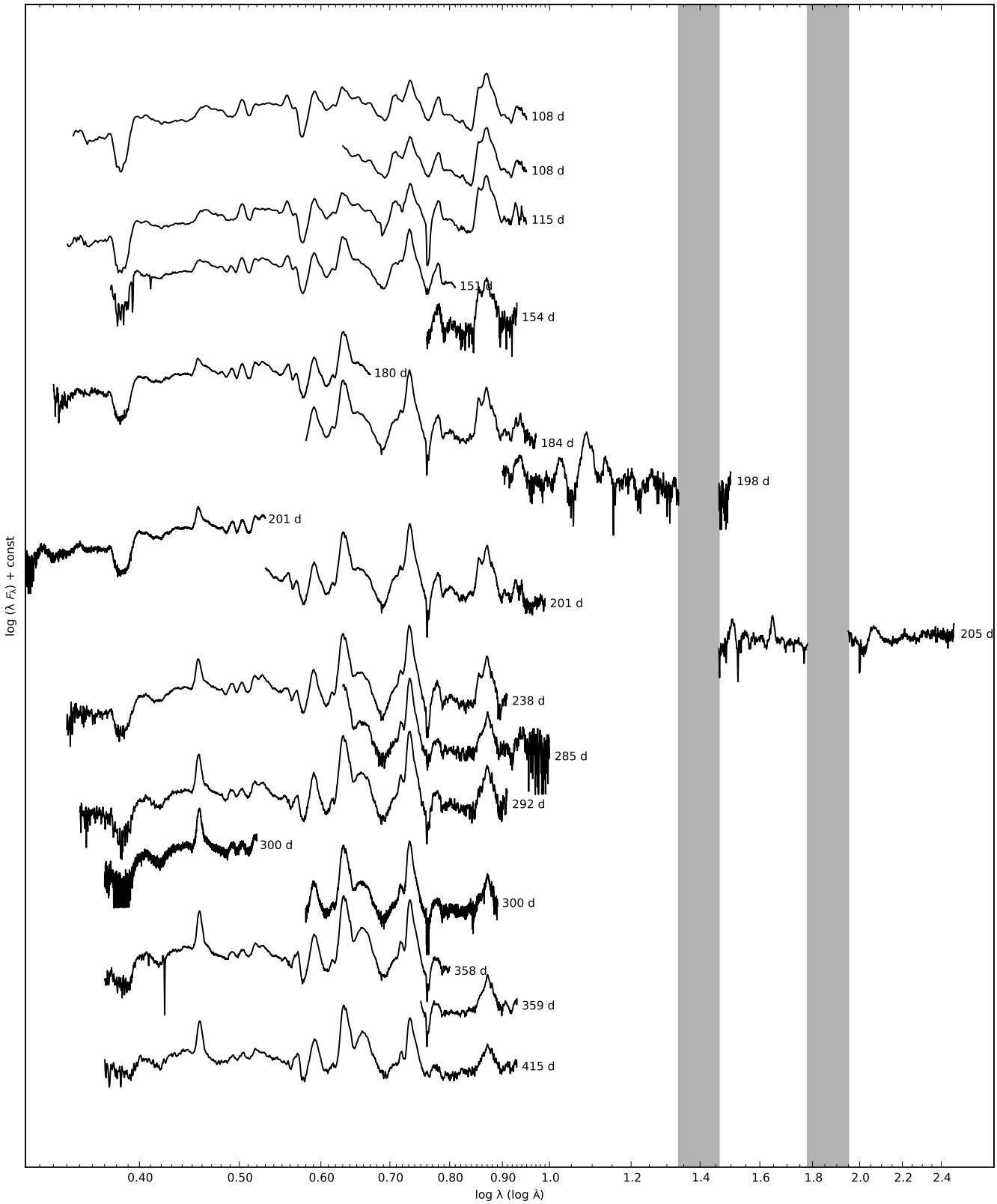

Fig. 3. Sequence of the observed late-time (100-415 days) spectra for SN 2011dh. Spectra obtained on the same night using the same telescope and instrument have been combined and each spectra have been labelled with the phase of the SN. Telluric absorption bands are marked with a ⊕ symbol in the optical and shown as grey regions in the NIR.

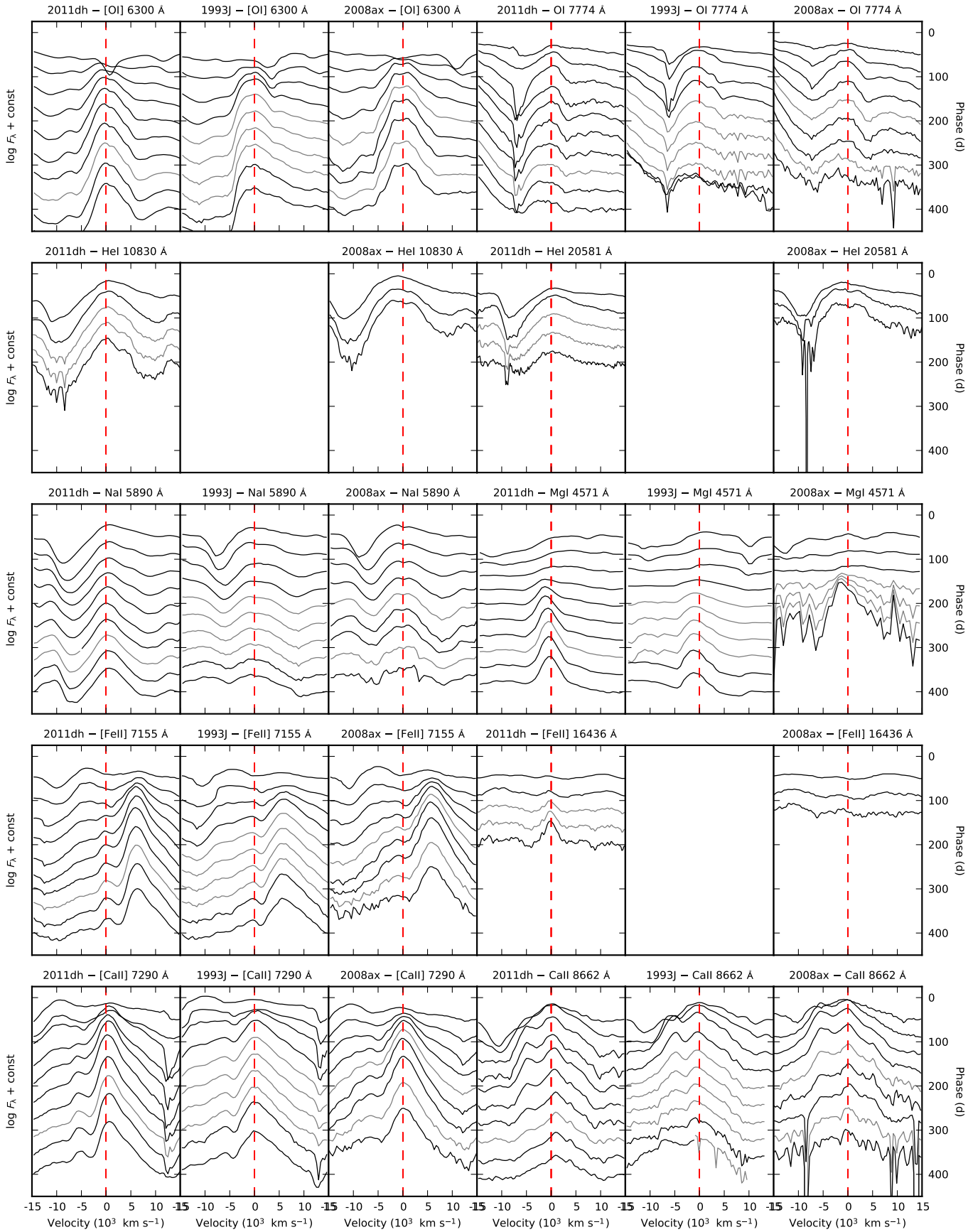

Fig. 20. Closeup of (interpolated) spectral evolution centred on the [O I] 6300 Å, [O I] 7774 Å, He I 10830 Å, He I 20581 Å, Na I 5890,5896 Å, Mg I 4571 Å, [Fe II] 7155 Å, [Fe II] 16436 Å, [Ca II 7291 Åand Ca II 8662 Å lines for SN 2011dh as compared to SNe 1993J and 2008ax.

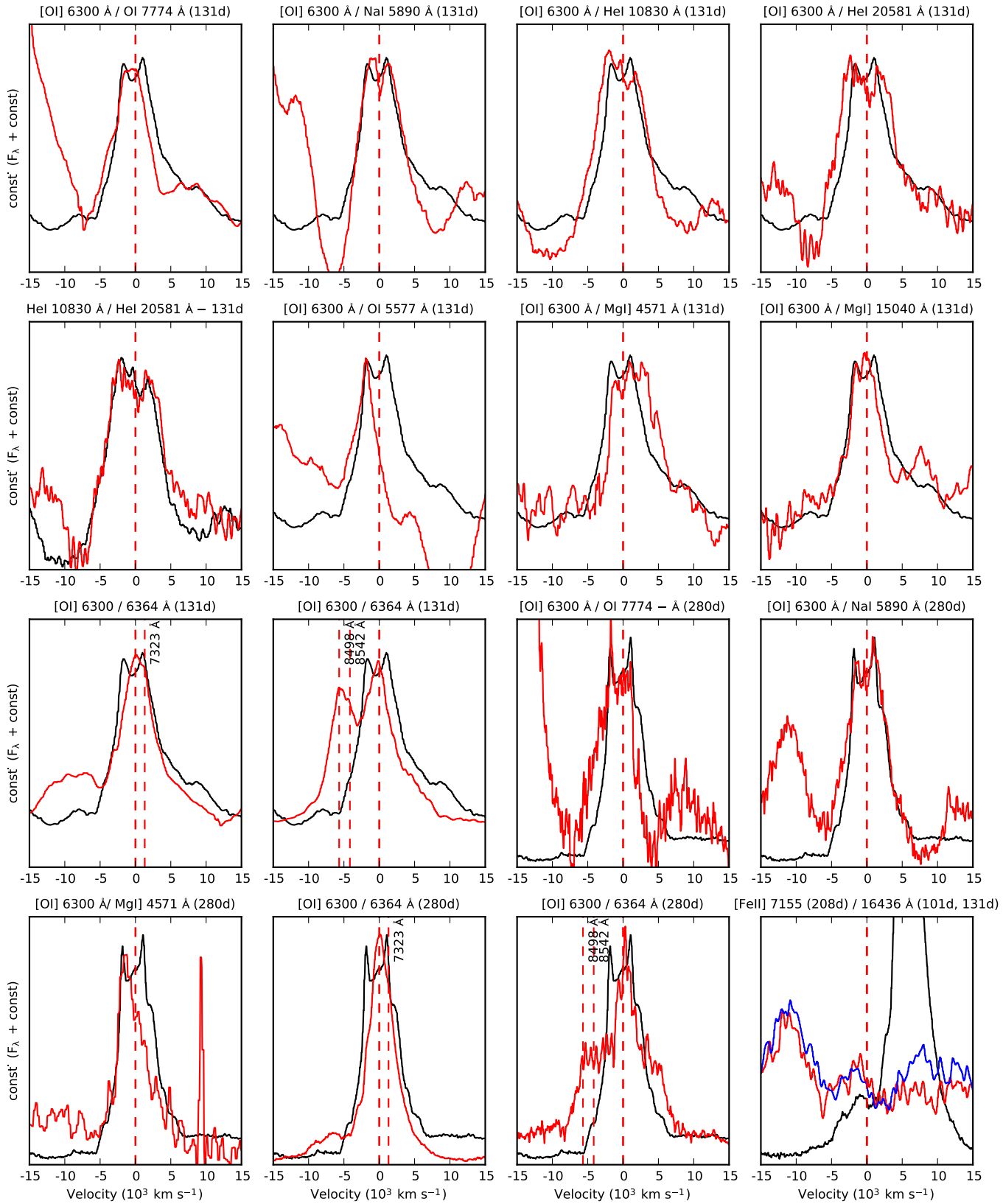

Fig. 21. Comparison of the [O I] 7774 Å, O I 5577 Å, Na I 5890,5896 Å, He I 10830 Å, He I 20581 Å, [Ca II 7291 Åand Ca II 8662 Å lines to the [O I] 6300 Åfor SN 2008ax at 131 and 280 days.

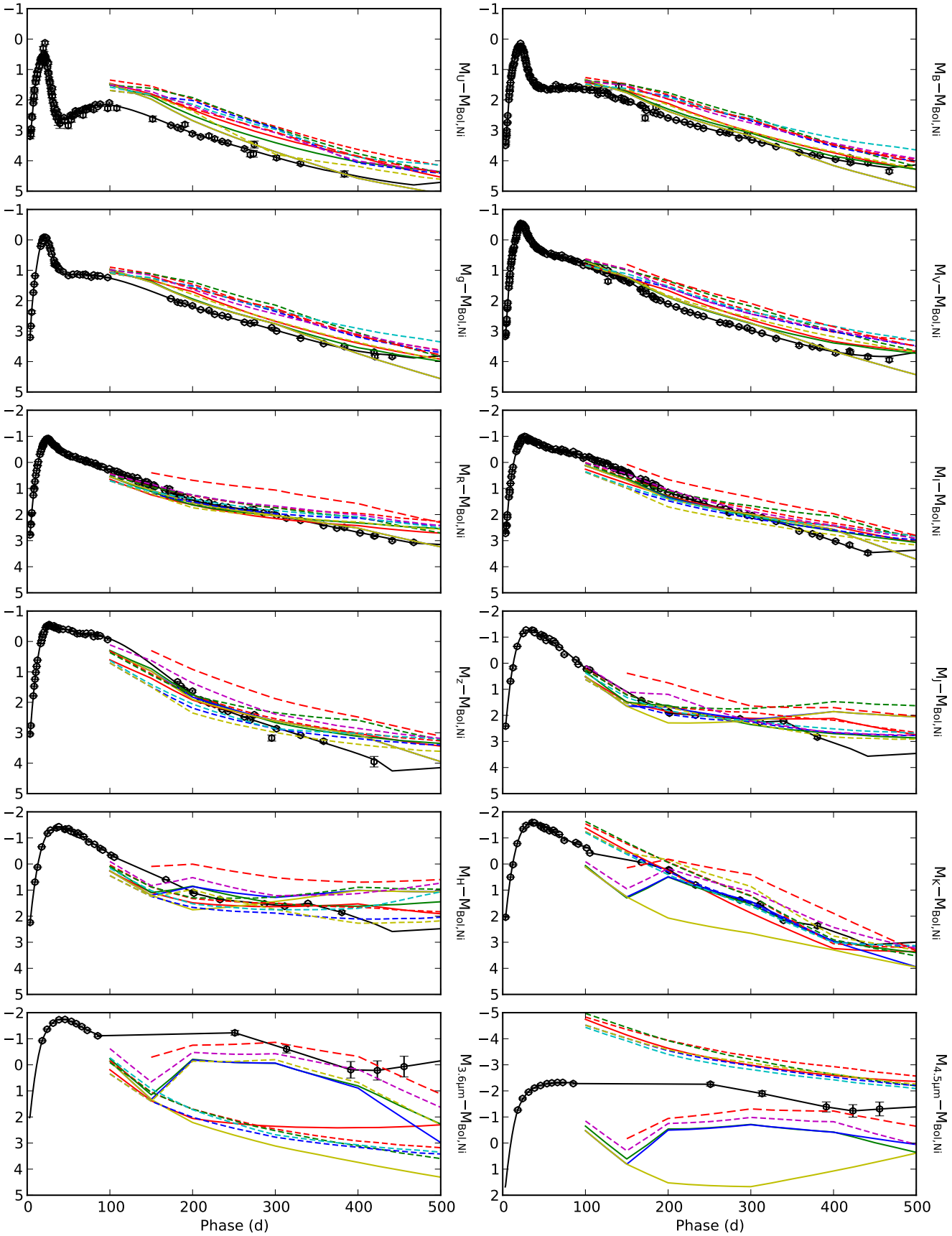

Fig. 25. Optical, NIR and MIR magnitudes for the J13 models as compared to the observed magnitudes. The lightcurves are displayed as in Fig. 24.

Table 4. Optical colour-corrected JC *U* and S-corrected JC *BVRI* magnitudes for SN 2011dh. Errors are given in parentheses. For simplicity data for the first 100 days already published in E13 are included.

JD (+2400000) (d)	Phase (d)	*U* (mag)	*B* (mag)	*V* (mag)	*R* (mag)	*I* (mag)	Telescope (Instrument)
55716.43	3.43	14.99 (0.03)	15.35 (0.02)	14.92 (0.02)	14.54 (0.01)	14.41 (0.02)	LT (RATCam)
55716.43	3.43	15.15 (0.08)	15.39 (0.02)	14.94 (0.02)	14.57 (0.01)	14.46 (0.01)	TNG (LRS)
55717.43	4.43	15.03 (0.03)	15.14 (0.02)	14.67 (0.03)	14.25 (0.01)	14.26 (0.03)	LT (RATCam)
55717.48	4.48	15.17 (0.09)	15.21 (0.03)	14.63 (0.03)	14.24 (0.01)	14.23 (0.02)	AS-1.82m (AFOSC)
55717.48	4.48	...	15.12 (0.03)	14.63 (0.02)	14.27 (0.01)	14.28 (0.02)	CANTAB (BIGST8)
55718.48	5.48	...	14.84 (0.01)	14.28 (0.02)	13.94 (0.01)	13.94 (0.01)	LT (RATCam)
55718.57	5.57	14.68 (0.06)	14.84 (0.02)	14.24 (0.02)	13.91 (0.01)	14.04 (0.01)	CA-2.2m (CAFOS)
55720.42	7.42	14.42 (0.02)	14.25 (0.01)	13.75 (0.03)	13.41 (0.01)	13.43 (0.02)	LT (RATCam)
55721.42	8.42	14.28 (0.10)	14.02 (0.01)	13.48 (0.01)	13.22 (0.01)	13.24 (0.02)	LT (RATCam)
55721.43	8.43	14.07 (0.07)	14.06 (0.01)	13.60 (0.04)	13.27 (0.02)	13.34 (0.02)	NOT (ALFOSC)
55722.42	9.42	...	13.86 (0.01)	13.29 (0.01)	13.05 (0.01)	13.07 (0.01)	LT (RATCam)
55723.41	10.41	13.98 (0.06)	13.71 (0.01)	13.16 (0.01)	12.89 (0.01)	12.90 (0.01)	LT (RATCam)
55724.41	11.41	13.91 (0.08)	13.62 (0.01)	13.03 (0.01)	12.79 (0.01)	12.77 (0.01)	LT (RATCam)
55725.39	12.39	...	...	12.94 (0.02)	12.66 (0.01)	...	MONTCAB (BIGST8)
55725.43	12.43	13.88 (0.07)	13.52 (0.02)	12.92 (0.04)	12.68 (0.01)	12.68 (0.01)	LT (RATCam)
55726.36	13.36	...	13.52 (0.01)	12.91 (0.02)	12.59 (0.01)	...	MONTCAB (BIGST8)
55728.40	15.40	...	13.39 (0.01)	12.77 (0.01)	12.44 (0.01)	...	MONTCAB (BIGST8)
55729.39	16.39	13.65 (0.01)	13.35 (0.01)	12.77 (0.06)	12.39 (0.01)	12.35 (0.02)	LT (RATCam)
55730.40	17.40	13.64 (0.03)	13.33 (0.01)	12.66 (0.01)	12.36 (0.01)	12.32 (0.01)	LT (RATCam)
55731.41	18.41	13.74 (0.09)	13.30 (0.01)	12.60 (0.02)	12.31 (0.01)	12.27 (0.01)	LT (RATCam)
55731.82	18.82	...	...	...	12.33 (0.02)	12.25 (0.01)	FTN (FS02)
55732.40	19.40	...	13.35 (0.03)	12.61 (0.01)	12.27 (0.01)	12.21 (0.01)	CANTAB (BIGST8)
55732.41	19.41	13.44 (0.06)	13.36 (0.02)	12.64 (0.02)	12.33 (0.02)	12.31 (0.02)	NOT (ALFOSC)
55732.46	19.46	13.71 (0.07)	13.32 (0.01)	12.58 (0.01)	12.28 (0.02)	12.22 (0.01)	LT (RATCam)
55733.45	20.45	13.67 (0.07)	...	...	12.26 (0.01)	12.20 (0.02)	LT (RATCam)
55734.52	21.52	13.37 (0.05)	13.33 (0.01)	12.58 (0.01)	12.25 (0.01)	12.29 (0.01)	CA-2.2m (CAFOS)
55735.44	22.44	13.91 (0.04)	...	...	12.26 (0.01)	12.16 (0.01)	LT (RATCam)
55736.44	23.44	14.13 (0.08)	...	...	12.26 (0.01)	12.16 (0.01)	LT (RATCam)
55737.39	24.39	...	13.65 (0.01)	12.72 (0.01)	...	...	LT (RATCam)
55738.42	25.42	14.50 (0.04)	13.79 (0.02)	12.81 (0.01)	12.32 (0.02)	12.22 (0.01)	LT (RATCam)
55738.51	25.51	14.20 (0.04)	13.77 (0.02)	12.82 (0.01)	12.38 (0.01)	12.26 (0.01)	NOT (ALFOSC)
55739.43	26.43	14.73 (0.04)	13.95 (0.02)	12.88 (0.01)	12.38 (0.01)	12.23 (0.01)	LT (RATCam)
55740.36	27.36	...	14.09 (0.04)	12.93 (0.01)	12.45 (0.01)	12.29 (0.01)	MONTCAB (BIGST8)
55740.43	27.43	14.91 (0.03)	14.12 (0.01)	12.97 (0.01)	12.48 (0.01)	12.30 (0.01)	LT (RATCam)
55740.44	27.44	...	...	12.97 (0.01)	12.47 (0.01)	...	TJO (MEIA)
55741.44	28.44	...	...	...	12.54 (0.01)	12.32 (0.01)	LT (RATCam)
55742.49	29.49	15.33 (0.01)	...	...	12.62 (0.01)	12.40 (0.01)	LT (RATCam)
55743.41	30.41	...	14.53 (0.01)	13.27 (0.02)	...	...	LT (RATCam)
55743.42	30.42	15.18 (0.05)	14.51 (0.02)	...	12.65 (0.01)	12.53 (0.01)	CA-2.2m (CAFOS)
55743.42	30.42	15.43 (0.05)	14.53 (0.01)	13.26 (0.03)	12.68 (0.01)	12.49 (0.01)	NOT (ALFOSC)
55745.39	32.39	15.74 (0.03)	14.74 (0.01)	13.44 (0.01)	12.77 (0.01)	12.56 (0.01)	NOT (ALFOSC)
55745.44	32.44	15.93 (0.04)	...	...	12.81 (0.01)	12.53 (0.01)	LT (RATCam)
55745.80	32.80	...	...	...	12.80 (0.01)	12.51 (0.01)	FTN (FS02)
55746.45	33.45	16.07 (0.04)	14.87 (0.03)	13.51 (0.01)	12.83 (0.01)	12.55 (0.02)	LT (RATCam)
55747.44	34.44	16.12 (0.04)	...	...	12.89 (0.01)	12.59 (0.01)	LT (RATCam)
55748.43	35.43	16.02 (0.02)	14.97 (0.01)	13.62 (0.01)	12.88 (0.01)	12.65 (0.01)	NOT (ALFOSC)
55748.44	35.44	16.27 (0.04)	...	...	12.94 (0.01)	12.62 (0.01)	LT (RATCam)
55750.40	37.40	16.20 (0.04)	15.10 (0.01)	13.73 (0.01)	13.03 (0.01)	12.73 (0.01)	NOT (ALFOSC)
55750.42	37.42	16.41 (0.14)	15.11 (0.02)	13.78 (0.03)	13.03 (0.01)	12.73 (0.02)	LT (RATCam)
55751.41	38.41	...	15.14 (0.01)	13.81 (0.01)	13.08 (0.01)	12.73 (0.01)	TJO (MEIA)
55751.43	38.43	...	...	...	13.11 (0.01)	12.77 (0.01)	LT (RATCam)
55752.45	39.45	16.54 (0.16)	...	...	13.13 (0.01)	12.75 (0.01)	LT (RATCam)

Table 3. Continued.

JD (+2400000) (d)	Phase (d)	U (mag)	B (mag)	V (mag)	R (mag)	I (mag)	Telescope (Instrument)
55753.42	40.42	...	15.29 (0.01)	13.90 (0.02)	...	...	LT (RATCam)
55753.46	40.46	16.45 (0.05)	15.24 (0.01)	13.86 (0.01)	13.15 (0.01)	12.81 (0.01)	NOT (ALFOSC)
55755.40	42.40	16.42 (0.04)	15.30 (0.01)	13.96 (0.01)	13.23 (0.01)	12.89 (0.01)	NOT (ALFOSC)
55756.44	43.44	...	15.28 (0.02)	13.98 (0.02)	13.28 (0.02)	12.86 (0.01)	AS-Schmidt (SBIG)
55756.45	43.45	...	15.38 (0.02)	13.98 (0.01)	13.27 (0.03)	12.92 (0.01)	LT (RATCam)
55757.43	44.43	16.42 (0.04)	15.38 (0.01)	14.05 (0.01)	13.29 (0.01)	12.97 (0.01)	NOT (ALFOSC)
55759.45	46.45	...	15.44 (0.01)	14.06 (0.02)	...	...	LT (RATCam)
55761.40	48.40	...	15.44 (0.01)	14.17 (0.01)	13.44 (0.01)	13.02 (0.01)	AS-Schmidt (SBIG)
55762.41	49.41	...	15.45 (0.01)	14.16 (0.01)	13.44 (0.01)	13.06 (0.01)	NOT (ALFOSC)
55762.78	49.78	...	...	...	13.44 (0.01)	13.03 (0.01)	FTN (FS02)
55763.44	50.44	...	15.47 (0.01)	14.22 (0.01)	13.47 (0.01)	13.09 (0.01)	AS-Schmidt (SBIG)
55765.43	52.43	16.44 (0.03)	15.52 (0.01)	14.26 (0.01)	13.55 (0.01)	13.17 (0.01)	NOT (ALFOSC)
55767.43	54.43	16.50 (0.05)	...	...	13.58 (0.01)	13.16 (0.02)	LT (RATCam)
55768.45	55.45	16.48 (0.04)	...	...	13.60 (0.02)	13.19 (0.02)	LT (RATCam)
55771.40	58.40	16.37 (0.03)	15.58 (0.01)	14.32 (0.01)	13.62 (0.01)	13.28 (0.01)	CA-2.2m (CAFOS)
55773.39	60.39	16.45 (0.04)	15.60 (0.01)	14.38 (0.01)	13.71 (0.01)	13.32 (0.01)	NOT (ALFOSC)
55776.38	63.38	16.47 (0.04)	15.64 (0.01)	14.46 (0.01)	13.77 (0.01)	13.36 (0.01)	NOT (ALFOSC)
55777.33	64.33	...	15.52 (0.03)	14.46 (0.02)	13.78 (0.02)	13.34 (0.02)	AS-Schmidt (SBIG)
55780.40	67.40	16.42 (0.03)	15.65 (0.01)	14.50 (0.01)	13.85 (0.01)	13.43 (0.01)	NOT (ALFOSC)
55783.43	70.43	16.41 (0.03)	15.71 (0.01)	14.58 (0.01)	13.94 (0.01)	13.51 (0.01)	NOT (ALFOSC)
55784.33	71.33	...	15.66 (0.02)	14.59 (0.01)	...	13.43 (0.02)	AS-Schmidt (SBIG)
55784.39	71.39	16.45 (0.04)	15.66 (0.01)	14.52 (0.02)	13.90 (0.01)	13.47 (0.02)	CA-2.2m (CAFOS)
55784.77	71.77	...	...	...	13.93 (0.02)	13.45 (0.01)	FTN (FS02)
55785.36	72.36	...	15.70 (0.02)	14.61 (0.01)	13.96 (0.01)	13.45 (0.01)	AS-Schmidt (SBIG)
55788.41	75.41	...	...	...	14.02 (0.02)	13.52 (0.01)	AS-Schmidt (SBIG)
55790.38	77.38	16.45 (0.09)	...	...	14.03 (0.01)	13.61 (0.01)	LT (RATCam)
55793.37	80.37	16.55 (0.07)	15.80 (0.01)	14.74 (0.01)	14.13 (0.01)	13.67 (0.01)	NOT (ALFOSC)
55795.35	82.35	16.40 (0.04)	15.78 (0.01)	14.76 (0.01)	14.12 (0.01)	13.68 (0.01)	CA-2.2m (CAFOS)
55797.37	84.37	...	15.83 (0.02)	14.82 (0.01)	...	...	AS-Schmidt (SBIG)
55797.76	84.76	...	...	...	14.22 (0.01)	13.68 (0.01)	FTN (FS02)
55798.36	85.36	16.50 (0.03)	15.84 (0.01)	14.84 (0.01)	14.25 (0.01)	13.65 (0.02)	NOT (ALFOSC)
55799.33	86.33	...	15.82 (0.01)	14.86 (0.01)	...	...	AS-Schmidt (SBIG)
55801.36	88.36	16.44 (0.04)	15.89 (0.01)	14.90 (0.01)	14.31 (0.01)	13.80 (0.01)	NOT (ALFOSC)
55801.40	88.40	...	15.80 (0.02)	14.90 (0.01)	...	...	AS-Schmidt (SBIG)
55803.35	90.35	...	15.88 (0.02)	14.91 (0.01)	14.32 (0.01)	13.79 (0.01)	AS-Schmidt (SBIG)
55805.33	92.33	...	15.87 (0.02)	14.97 (0.02)	14.37 (0.01)	13.83 (0.01)	AS-Schmidt (SBIG)
55810.34	97.34	16.68 (0.06)	16.00 (0.01)	15.11 (0.01)	14.52 (0.01)	14.02 (0.01)	NOT (ALFOSC)
55812.33	99.33	16.51 (0.03)	16.02 (0.01)	15.05 (0.01)	14.49 (0.01)	14.00 (0.01)	CA-2.2m (CAFOS)
55817.35	104.35	...	16.02 (0.03)	15.19 (0.02)	14.63 (0.02)	14.04 (0.02)	AS-Schmidt (SBIG)
55818.33	105.33	...	16.10 (0.02)	15.19 (0.02)	14.66 (0.01)	14.08 (0.01)	AS-Schmidt (SBIG)
55821.31	108.31	16.77 (0.08)	16.12 (0.02)	15.25 (0.01)	14.68 (0.01)	14.16 (0.01)	CA-2.2m (CAFOS)
55824.32	111.32	...	...	15.31 (0.02)	14.75 (0.03)	14.24 (0.03)	AS-Schmidt (SBIG)
55827.33	114.33	...	16.16 (0.03)	15.42 (0.01)	14.87 (0.02)	14.27 (0.01)	AS-Schmidt (SBIG)
55827.48	114.48	...	16.22 (0.07)	15.37 (0.03)	14.94 (0.05)	14.38 (0.05)	AT (ANDOR)
55828.27	115.27	...	16.34 (0.04)	15.39 (0.02)	14.86 (0.02)	14.31 (0.01)	AT (ANDOR)
55830.28	117.28	...	16.30 (0.02)	15.38 (0.01)	14.91 (0.01)	14.34 (0.01)	AS-1.82m (AFOSC)
55834.26	121.26	...	16.23 (0.03)	15.49 (0.02)	14.99 (0.02)	14.44 (0.02)	AT (ANDOR)
55834.31	121.31	...	16.35 (0.02)	15.55 (0.01)	14.99 (0.02)	14.41 (0.02)	AS-Schmidt (SBIG)
55838.34	125.34	...	...	15.64 (0.02)	15.11 (0.03)	14.49 (0.01)	AS-Schmidt (SBIG)
55839.28	126.28	...	16.39 (0.03)	15.65 (0.02)	15.12 (0.02)	14.52 (0.02)	AS-Schmidt (SBIG)
55840.26	127.26	...	16.44 (0.03)	15.57 (0.02)	15.15 (0.03)	14.53 (0.02)	AT (ANDOR)
55840.30	127.30	...	16.44 (0.14)	15.93 (0.06)	15.08 (0.04)	14.59 (0.04)	AS-Schmidt (SBIG)

Table 3. Continued.

JD (+2400000) (d)	Phase (d)	U (mag)	B (mag)	V (mag)	R (mag)	I (mag)	Telescope (Instrument)
55846.26	133.26	...	16.60 (0.03)	15.77 (0.02)	15.17 (0.02)	14.71 (0.02)	AT (ANDOR)
55847.30	134.30	...	...	15.81 (0.02)	15.35 (0.03)	14.77 (0.02)	AT (ANDOR)
55849.26	136.26	...	16.68 (0.05)	15.81 (0.02)	15.33 (0.03)	14.75 (0.02)	AT (ANDOR)
55853.27	140.27	...	16.32 (0.06)	15.90 (0.05)	15.44 (0.05)	14.91 (0.04)	AS-Schmidt (SBIG)
55855.38	142.38	...	...	15.96 (0.03)	15.44 (0.03)	14.93 (0.03)	AT (ANDOR)
55856.24	143.24	...	16.72 (0.06)	16.01 (0.03)	15.42 (0.02)	14.91 (0.02)	AT (ANDOR)
55858.29	145.29	...	...	16.02 (0.03)	15.45 (0.03)	14.96 (0.02)	AT (ANDOR)
55859.23	146.23	...	16.84 (0.05)	16.08 (0.02)	15.56 (0.03)	15.01 (0.02)	AT (ANDOR)
55860.22	147.22	...	16.80 (0.05)	16.10 (0.03)	15.53 (0.03)	15.02 (0.02)	AT (ANDOR)
55864.69	151.69	17.55 (0.09)	16.94 (0.02)	16.14 (0.01)	15.65 (0.01)	15.10 (0.01)	AS-1.82m (AFOSC)
55866.28	153.28	...	...	16.23 (0.02)	15.64 (0.03)	15.18 (0.02)	AT (ANDOR)
55867.70	154.70	...	16.97 (0.02)	16.21 (0.03)	15.71 (0.02)	15.25 (0.02)	CA-2.2m (CAFOS)
55879.66	166.66	...	17.19 (0.03)	16.58 (0.02)	15.99 (0.02)	15.49 (0.02)	AS-Schmidt (SBIG)
55881.74	168.74	...	17.23 (0.02)	16.59 (0.02)	15.94 (0.01)	15.66 (0.03)	CA-2.2m (CAFOS)
55883.24	170.24	...	...	16.72 (0.05)	16.19 (0.05)	15.61 (0.02)	AT (ANDOR)
55885.21	172.21	...	17.67 (0.10)	16.53 (0.03)	15.98 (0.05)	15.62 (0.03)	AT (ANDOR)
55885.73	172.73	...	17.36 (0.08)	16.67 (0.02)	...	15.59 (0.03)	AS-1.82m (AFOSC)
55886.75	173.75	17.97 (0.03)	17.43 (0.01)	16.79 (0.01)	16.17 (0.01)	15.73 (0.01)	NOT (ALFOSC)
55893.71	180.71	...	...	16.93 (0.02)	16.27 (0.01)	15.80 (0.02)	AS-Schmidt (SBIG)
55894.76	181.76	18.12 (0.03)	17.58 (0.01)	16.96 (0.01)	16.31 (0.01)	15.89 (0.01)	NOT (ALFOSC)
55896.20	183.20	...	...	17.03 (0.05)	16.44 (0.06)	16.01 (0.04)	AT (ANDOR)
55898.19	185.19	...	17.44 (0.08)	17.06 (0.04)	16.35 (0.04)	15.90 (0.03)	AT (ANDOR)
55898.73	185.73	18.20 (0.04)	17.65 (0.01)	17.09 (0.01)	16.39 (0.01)	16.05 (0.01)	NOT (ALFOSC)
55903.76	190.76	18.11 (0.06)	17.74 (0.02)	17.18 (0.02)	16.48 (0.01)	16.10 (0.02)	NOT (ALFOSC)
55912.79	199.79	18.51 (0.05)	17.93 (0.02)	17.37 (0.01)	16.68 (0.01)	16.33 (0.01)	NOT (ALFOSC)
55922.76	209.76	18.70 (0.03)	18.10 (0.01)	17.57 (0.01)	16.86 (0.01)	16.52 (0.01)	NOT (ALFOSC)
55932.79	219.79	18.77 (0.06)	18.26 (0.01)	17.80 (0.02)	16.97 (0.02)	16.72 (0.02)	NOT (ALFOSC)
55939.73	226.73	18.93 (0.05)	18.40 (0.02)	17.92 (0.02)	17.12 (0.01)	16.85 (0.01)	NOT (ALFOSC)
55948.73	235.73	19.11 (0.04)	18.56 (0.01)	18.08 (0.01)	17.27 (0.01)	17.04 (0.01)	NOT (ALFOSC)
55955.76	242.76	19.23 (0.04)	18.69 (0.01)	18.20 (0.01)	17.37 (0.01)	17.19 (0.01)	NOT (ALFOSC)
55975.69	262.69	19.61 (0.05)	19.01 (0.01)	18.59 (0.01)	17.67 (0.01)	17.51 (0.01)	NOT (ALFOSC)
55982.74	269.74	19.88 (0.07)	19.09 (0.02)	18.69 (0.02)	17.74 (0.01)	17.65 (0.01)	NOT (ALFOSC)
55986.62	273.62	19.88 (0.11)	19.15 (0.03)	18.75 (0.03)	17.76 (0.02)	17.83 (0.03)	CA-2.2m (CAFOS)
55987.62	274.62	19.59 (0.12)	19.11 (0.02)	18.76 (0.02)	17.78 (0.01)	17.78 (0.01)	LT (RATCam)
55998.67	285.67	...	19.43 (0.02)	18.96 (0.02)	18.00 (0.01)	17.95 (0.01)	NOT (ALFOSC)
56008.66	295.66	...	19.40 (0.03)	19.10 (0.03)	18.06 (0.02)	18.14 (0.03)	LT (RATCam)
56014.51	301.51	20.28 (0.07)	19.65 (0.01)	19.24 (0.02)	18.26 (0.01)	18.22 (0.01)	NOT (ALFOSC)
56026.49	313.49	...	19.86 (0.02)	19.44 (0.02)	18.47 (0.01)	18.41 (0.02)	NOT (ALFOSC)
56043.59	330.59	20.76 (0.06)	20.15 (0.02)	19.78 (0.02)	18.72 (0.01)	18.72 (0.02)	NOT (ALFOSC)
56071.42	358.42	...	20.61 (0.02)	20.28 (0.04)	19.20 (0.02)	19.36 (0.03)	NOT (ALFOSC)
56087.43	374.43	...	20.86 (0.02)	20.48 (0.03)	19.45 (0.02)	19.62 (0.02)	NOT (ALFOSC)
56096.48	383.48	21.62 (0.10)	20.95 (0.03)	20.60 (0.04)	19.51 (0.02)	19.81 (0.03)	NOT (ALFOSC)
56115.44	402.44	...	21.26 (0.03)	20.96 (0.05)	19.91 (0.02)	20.18 (0.04)	NOT (ALFOSC)
56132.43	419.43	...	21.38 (0.06)	21.07 (0.06)	20.19 (0.03)	20.49 (0.05)	NOT (ALFOSC)
56133.40	420.40	...	21.55 (0.05)	21.13 (0.06)	20.19 (0.03)	...	NOT (ALFOSC)
56154.39	441.39	...	21.76 (0.05)	21.46 (0.06)	20.58 (0.04)	21.01 (0.08)	NOT (ALFOSC)
56180.37	467.37	...	22.30 (0.05)	21.82 (0.06)	20.90 (0.04)	...	NOT (ALFOSC)
56313.73	600.73	...	...	22.44 (0.10)	...	...	NOT (ALFOSC)
56353.50	640.50	...	...	23.02 (0.00)	...	22.58 (0.00)	HST (ACS)
56371.69	658.69	...	23.42 (0.32)	...	...	...	NOT (ALFOSC)
56397.64	684.64	...	...	23.20 (0.20)	...	...	NOT (ALFOSC)
56445.43	732.43	...	23.96 (0.50)	...	...	...	NOT (ALFOSC)

Table 4. Optical colour-corrected SDSS *u* and S-corrected SDSS *griz* magnitudes for SN 2011dh. Errors are given in parentheses. For simplicity data for the first 100 days already published in E13 are included.

JD (+2400000) (d)	Phase (d)	*u* (mag)	*g* (mag)	*r* (mag)	*i* (mag)	*z* (mag)	Telescope (Instrument)
55716.47	3.47	15.90 (0.03)	15.08 (0.01)	14.68 (0.01)	14.80 (0.01)	14.76 (0.02)	LT (RATCam)
55717.46	4.46	16.01 (0.03)	14.80 (0.01)	14.38 (0.01)	14.61 (0.01)	14.58 (0.02)	LT (RATCam)
55718.53	5.53	...	14.44 (0.04)	14.06 (0.01)	14.27 (0.01)	...	LT (RATCam)
55720.44	7.44	15.39 (0.02)	13.97 (0.01)	13.53 (0.01)	13.73 (0.02)	13.87 (0.01)	LT (RATCam)
55721.44	8.44	15.09 (0.01)	13.78 (0.01)	13.33 (0.01)	13.52 (0.01)	13.64 (0.01)	LT (RATCam)
55722.44	9.44	...	13.59 (0.01)	13.18 (0.01)	13.35 (0.01)	13.49 (0.01)	LT (RATCam)
55723.41	10.41	14.82 (0.03)	...	13.02 (0.01)	13.16 (0.01)	13.34 (0.01)	LT (RATCam)
55724.41	11.41	14.72 (0.02)	...	12.93 (0.01)	13.05 (0.01)	13.22 (0.01)	LT (RATCam)
55725.43	12.43	14.74 (0.04)	...	12.83 (0.01)	12.94 (0.01)	13.09 (0.01)	LT (RATCam)
55729.39	16.39	14.56 (0.03)	13.10 (0.01)	12.56 (0.01)	12.62 (0.01)	12.81 (0.01)	LT (RATCam)
55730.40	17.40	14.45 (0.03)	13.07 (0.01)	12.51 (0.01)	12.56 (0.01)	12.77 (0.01)	LT (RATCam)
55731.41	18.41	14.54 (0.03)	13.02 (0.01)	12.46 (0.01)	12.51 (0.01)	12.71 (0.01)	LT (RATCam)
55731.82	18.82	...	13.07 (0.01)	12.46 (0.01)	12.50 (0.01)	12.65 (0.01)	FTN (FS02)
55732.46	19.46	14.56 (0.01)	13.00 (0.03)	12.42 (0.01)	12.48 (0.01)	12.67 (0.01)	LT (RATCam)
55733.45	20.45	14.52 (0.05)	13.03 (0.01)	12.41 (0.01)	12.45 (0.01)	12.65 (0.01)	LT (RATCam)
55735.44	22.44	14.75 (0.04)	13.12 (0.01)	12.43 (0.01)	12.41 (0.01)	12.60 (0.01)	LT (RATCam)
55736.44	23.44	14.96 (0.03)	13.19 (0.02)	12.45 (0.01)	12.42 (0.01)	12.59 (0.02)	LT (RATCam)
55738.45	25.45	15.37 (0.02)	13.43 (0.01)	12.55 (0.01)	12.47 (0.01)	12.65 (0.01)	LT (RATCam)
55739.44	26.44	15.55 (0.02)	13.50 (0.03)	12.59 (0.01)	12.50 (0.01)	12.65 (0.01)	LT (RATCam)
55740.44	27.44	15.80 (0.01)	13.66 (0.01)	12.66 (0.01)	12.55 (0.01)	12.70 (0.01)	LT (RATCam)
55741.44	28.44	...	13.75 (0.02)	12.76 (0.01)	12.59 (0.02)	12.76 (0.01)	LT (RATCam)
55742.49	29.49	16.20 (0.02)	13.92 (0.01)	12.84 (0.01)	12.65 (0.01)	12.80 (0.01)	LT (RATCam)
55745.44	32.44	16.71 (0.05)	14.20 (0.02)	13.04 (0.01)	12.79 (0.01)	12.87 (0.03)	LT (RATCam)
55745.80	32.80	...	14.35 (0.04)	13.00 (0.01)	12.79 (0.01)	12.94 (0.01)	FTN (FS02)
55746.45	33.45	16.83 (0.04)	14.32 (0.01)	13.09 (0.01)	12.82 (0.01)	12.94 (0.01)	LT (RATCam)
55747.44	34.44	16.90 (0.04)	14.40 (0.02)	13.13 (0.01)	12.86 (0.01)	12.95 (0.01)	LT (RATCam)
55748.44	35.44	17.09 (0.04)	14.42 (0.02)	13.19 (0.01)	12.90 (0.01)	13.01 (0.01)	LT (RATCam)
55750.44	37.44	17.20 (0.10)	14.55 (0.02)	13.29 (0.01)	13.02 (0.02)	13.04 (0.04)	LT (RATCam)
55751.43	38.43	17.14 (0.03)	14.64 (0.03)	13.36 (0.01)	13.04 (0.01)	13.11 (0.01)	LT (RATCam)
55752.45	39.45	17.24 (0.07)	14.66 (0.01)	13.39 (0.01)	13.04 (0.01)	13.09 (0.01)	LT (RATCam)
55756.46	43.46	...	14.79 (0.01)	13.55 (0.01)	13.22 (0.01)	13.19 (0.01)	LT (RATCam)
55762.78	49.78	...	15.00 (0.02)	13.68 (0.01)	13.37 (0.01)	13.28 (0.01)	FTN (FS02)
55767.43	54.43	17.30 (0.02)	15.03 (0.01)	13.84 (0.01)	13.52 (0.01)	13.38 (0.02)	LT (RATCam)
55768.45	55.45	17.29 (0.02)	15.03 (0.01)	13.86 (0.01)	13.56 (0.01)	13.41 (0.01)	LT (RATCam)
55773.39	60.39	17.27 (0.04)	15.07 (0.01)	13.99 (0.01)	13.72 (0.01)	13.54 (0.02)	NOT (ALFOSC)
55776.38	63.38	17.36 (0.03)	15.13 (0.01)	14.03 (0.01)	13.76 (0.01)	13.56 (0.01)	NOT (ALFOSC)
55780.41	67.41	17.33 (0.03)	15.16 (0.01)	14.09 (0.01)	13.84 (0.01)	13.61 (0.01)	NOT (ALFOSC)
55783.44	70.44	17.26 (0.04)	15.18 (0.01)	14.19 (0.01)	13.93 (0.01)	13.67 (0.01)	NOT (ALFOSC)
55784.77	71.77	...	15.23 (0.02)	14.16 (0.01)	13.88 (0.01)	13.64 (0.01)	FTN (FS02)
55790.38	77.38	17.29 (0.03)	15.35 (0.04)	14.28 (0.01)	14.04 (0.01)	13.69 (0.02)	LT (RATCam)
55793.37	80.37	17.32 (0.03)	15.30 (0.01)	14.39 (0.01)	14.16 (0.01)	13.84 (0.01)	NOT (ALFOSC)
55797.76	84.76	...	15.38 (0.01)	14.42 (0.01)	14.18 (0.01)	13.82 (0.01)	FTN (FS02)
55798.37	85.37	17.35 (0.03)	15.38 (0.01)	14.50 (0.01)	14.26 (0.01)	13.87 (0.01)	NOT (ALFOSC)
55801.36	88.36	17.34 (0.01)	15.42 (0.01)	14.53 (0.01)	14.31 (0.01)	13.89 (0.01)	NOT (ALFOSC)
55810.34	97.34	17.49 (0.02)	15.55 (0.01)	14.75 (0.01)	14.56 (0.01)	14.10 (0.02)	NOT (ALFOSC)
55886.75	173.75	21.74 (1.97)	16.99 (0.01)	16.36 (0.01)	16.16 (0.01)	...	NOT (ALFOSC)
55894.76	181.76	18.89 (0.03)	17.19 (0.02)	16.50 (0.01)	16.28 (0.02)	16.31 (0.02)	NOT (ALFOSC)
55898.73	185.73	18.97 (0.03)	17.25 (0.01)	16.59 (0.01)	16.42 (0.01)	16.49 (0.01)	NOT (ALFOSC)
55903.76	190.76	19.07 (0.05)	17.32 (0.02)	16.68 (0.01)	16.47 (0.01)	16.68 (0.04)	NOT (ALFOSC)
55912.79	199.79	19.28 (0.04)	17.48 (0.02)	16.86 (0.01)	16.66 (0.01)	16.79 (0.03)	NOT (ALFOSC)

Table 5. Continued.

JD (+2400000) (d)	Phase (d)	u (mag)	g (mag)	r (mag)	i (mag)	z (mag)	Telescope (Instrument)
55922.77	209.77	19.44 (0.02)	17.71 (0.01)	17.05 (0.01)	16.83 (0.01)	17.18 (0.01)	NOT (ALFOSC)
55932.79	219.79	19.50 (0.05)	17.83 (0.02)	17.18 (0.02)	17.01 (0.02)	17.37 (0.04)	NOT (ALFOSC)
55939.74	226.74	19.74 (0.05)	18.02 (0.01)	17.31 (0.01)	17.11 (0.01)	17.49 (0.02)	NOT (ALFOSC)
55948.73	235.73	19.87 (0.03)	18.15 (0.01)	17.45 (0.01)	17.27 (0.01)	17.74 (0.01)	NOT (ALFOSC)
55955.76	242.76	20.01 (0.03)	18.27 (0.01)	17.57 (0.01)	17.40 (0.01)	17.87 (0.02)	NOT (ALFOSC)
55975.69	262.69	20.37 (0.04)	18.64 (0.01)	17.84 (0.01)	17.71 (0.01)	18.25 (0.02)	NOT (ALFOSC)
55982.74	269.74	20.64 (0.05)	18.74 (0.01)	17.92 (0.01)	17.86 (0.01)	18.42 (0.03)	NOT (ALFOSC)
55987.62	274.62	20.47 (0.11)	18.76 (0.01)	17.95 (0.01)	17.96 (0.01)	18.30 (0.03)	LT (RATCam)
56008.66	295.66	...	19.14 (0.02)	18.22 (0.01)	18.33 (0.03)	19.27 (0.10)	LT (RATCam)
56014.52	301.52	21.28 (0.04)	19.30 (0.01)	18.40 (0.01)	18.45 (0.01)	19.02 (0.02)	NOT (ALFOSC)
56043.60	330.60	21.73 (0.03)	19.82 (0.01)	18.82 (0.01)	18.96 (0.01)	19.52 (0.03)	NOT (ALFOSC)
56071.43	358.43	21.85 (0.06)	20.27 (0.02)	19.26 (0.02)	19.62 (0.03)	19.98 (0.05)	NOT (ALFOSC)
56096.49	383.49	22.35 (0.05)	20.61 (0.02)	19.55 (0.02)	20.09 (0.03)	...	NOT (ALFOSC)
56132.43	419.43	...	21.14 (0.03)	20.21 (0.03)	20.79 (0.05)	21.25 (0.17)	NOT (ALFOSC)
56133.41	420.41	...	21.30 (0.04)	20.21 (0.03)	20.95 (0.06)	...	NOT (ALFOSC)
56154.39	441.39	...	21.50 (0.04)	20.61 (0.03)	21.32 (0.07)	...	NOT (ALFOSC)
56313.75	600.75	...	...	22.46 (0.11)	...	...	NOT (ALFOSC)
56428.46	715.46	...	...	23.10 (0.20)	...	...	NOT (ALFOSC)

Table 6. NIR S-corrected 2MASS *JHK* magnitudes for SN 2011dh. Errors are given in parentheses. For simplicity data for the first 100 days already published in E13 are included.

JD (+2400000) (d)	Phase (d)	*J* (mag)	*H* (mag)	*K* (mag)	Telescope (Instrument)
55716.51	3.51	14.09 (0.01)	13.90 (0.01)	13.68 (0.02)	TNG (NICS)
55722.40	9.40	12.89 (0.01)	12.87 (0.01)	12.67 (0.01)	TNG (NICS)
55725.50	12.50	12.61 (0.04)	12.54 (0.01)	12.43 (0.02)	NOT (NOTCAM)
55730.51	17.51	12.12 (0.01)	12.08 (0.01)	11.94 (0.01)	TNG (NICS)
55737.72	24.72	11.96 (0.01)	11.90 (0.01)	11.72 (0.03)	LBT (LUCIFER)
55741.13	28.13	11.94 (0.01)	11.90 (0.02)	11.70 (0.05)	TCS (CAIN)
55748.43	35.43	12.14 (0.01)	12.00 (0.02)	11.77 (0.01)	TCS (CAIN)
55750.42	37.42	12.19 (0.01)	12.00 (0.01)	11.84 (0.04)	TCS (CAIN)
55751.42	38.42	12.29 (0.01)	12.01 (0.01)	11.84 (0.03)	TCS (CAIN)
55758.45	45.45	12.55 (0.01)	12.22 (0.01)	12.06 (0.01)	TNG (NICS)
55759.41	46.41	12.49 (0.03)	12.22 (0.03)	12.11 (0.04)	TCS (CAIN)
55762.41	49.41	12.57 (0.01)	12.26 (0.01)	12.17 (0.03)	TCS (CAIN)
55763.42	50.42	12.62 (0.02)	12.27 (0.04)	12.25 (0.06)	TCS (CAIN)
55765.45	52.45	12.79 (0.01)	12.38 (0.01)	12.23 (0.01)	TNG (NICS)
55769.41	56.41	12.77 (0.01)	12.48 (0.06)	12.40 (0.03)	TCS (CAIN)
55773.37	60.37	12.94 (0.03)	12.58 (0.01)	12.42 (0.02)	TNG (NICS)
55774.40	61.40	12.90 (0.01)	12.55 (0.03)	12.43 (0.04)	TCS (CAIN)
55776.40	63.40	13.00 (0.01)	12.64 (0.01)	12.53 (0.02)	TCS (CAIN)
55781.41	68.41	13.23 (0.01)	12.76 (0.01)	12.66 (0.01)	WHT (LIRIS)
55787.44	74.44	13.56 (0.03)	13.03 (0.02)	12.95 (0.02)	NOT (NOTCAM)
55801.36	88.36	13.90 (0.02)	13.41 (0.02)	13.17 (0.01)	TNG (NICS)
55804.34	91.34	14.10 (0.01)	13.50 (0.01)	13.26 (0.01)	CA-3.5m (O2000)
55814.32	101.32	14.38 (0.01)	13.80 (0.01)	13.50 (0.01)	CA-3.5m (O2000)
55818.36	105.36	14.45 (0.02)	13.91 (0.01)	13.74 (0.01)	NOT (NOTCAM)
55880.72	167.72	16.23 (0.01)	15.38 (0.01)	14.70 (0.01)	CA-3.5m (O2000)
55913.68	200.68	17.00 (0.01)	16.19 (0.02)	15.31 (0.02)	CA-3.5m (O2000)
55914.66	201.66	17.05 (0.01)	16.23 (0.02)	15.35 (0.02)	CA-3.5m (O2000)
55946.13	233.13	17.43 (0.02)	16.78 (0.02)	16.21 (0.02)	UKIRT (WFCAM)
55999.91	286.91	18.10 (0.02)	17.47 (0.02)	17.31 (0.02)	UKIRT (WFCAM)
56024.38	311.38	18.46 (0.03)	17.80 (0.03)	17.71 (0.04)	WHT (LIRIS)
56052.47	339.47	18.69 (0.02)	17.96 (0.02)	18.60 (0.03)	WHT (LIRIS)
56093.48	380.48	19.71 (0.06)	18.71 (0.06)	19.21 (0.08)	WHT (LIRIS)

Table 7. MIR Spitzer 3.6 μm and 4.5 μm magnitudes for SN 2011dh. Errors are given in parentheses. For simplicity data for the first 100 days already published in E13 are included.

JD (+2400000) (d)	Phase (d)	3.6 μm (mag)	4.5 μm (mag)	Telescope (Instrument)
55731.21	18.21	11.83 (0.02)	11.48 (0.02)	SPITZER (IRAC)
55737.06	24.06	11.66 (0.02)	11.31 (0.02)	SPITZER (IRAC)
55744.32	31.32	11.66 (0.02)	11.30 (0.02)	SPITZER (IRAC)
55751.46	38.46	11.68 (0.02)	11.30 (0.02)	SPITZER (IRAC)
55758.75	45.75	11.79 (0.02)	11.32 (0.02)	SPITZER (IRAC)
55766.45	53.45	11.96 (0.02)	11.34 (0.02)	SPITZER (IRAC)
55772.33	59.33	12.11 (0.03)	11.38 (0.02)	SPITZER (IRAC)
55779.12	66.12	12.30 (0.03)	11.43 (0.02)	SPITZER (IRAC)
55785.60	72.60	12.50 (0.03)	11.50 (0.02)	SPITZER (IRAC)
55798.28	85.28	12.84 (0.04)	11.66 (0.03)	SPITZER (IRAC)
55964.14	251.14	14.34 (0.09)	13.31 (0.07)	SPITZER (IRAC)
56026.63	313.63	15.57 (0.15)	14.27 (0.11)	SPITZER (IRAC)
56104.23	391.23	17.12 (0.32)	15.54 (0.19)	SPITZER (IRAC)
56136.41	423.41	17.46 (0.37)	16.01 (0.24)	SPITZER (IRAC)
56168.69	455.69	17.63 (0.40)	16.25 (0.26)	SPITZER (IRAC)
56337.59	624.59	18.42 (0.57)	17.59 (0.49)	SPITZER (IRAC)

Table 8. List of late-time (100-415 days) optical and NIR spectroscopic observations.

JD (+2400000) (d)	Phase (d)	Grism	Range (Å)	Resolution	Resolution (Å)	Telescope (Instrument)
55821.33	108.33	b200	3300-8700	...	12.0	CA-2.2m (CAFOS)
55821.33	108.33	r200	6300-10500	...	12.0	CA-2.2m (CAFOS)
55828.35	115.35	R300B	3200-5300	...	4.1	WHT (ISIS)
55828.35	115.35	R158R	5300-10000	...	7.7	WHT (ISIS)
55864.65	151.65	?	?-?	?	?	AS-1.22m (AFOSC)
55867.71	154.71	?	?-?	...	?	CA-2.2m (CAFOS)
55893.76	180.76	Grism 3	3200-6700	345	12.4	NOT (ALFOSC)
55897.76	184.76	Grism 5	5000-10250	415	16.8	NOT (ALFOSC)
55911.20	198.20	zJ	8900-15100	700	...	WHT (LIRIS)
55914.70	201.70	R300B	3200-5300	...	8.2	WHT (ISIS)
55914.70	201.70	R158R	5300-10000	...	15.4	WHT (ISIS)
55918.69	205.69	HK	14000-25000	333	...	TNG (NICS)
55951.64	238.64	Grism 4	3200-9100	355	16.2	NOT (ALFOSC)
55998.68	285.68	r200	6300-10500	...	12.0	CA-2.2m (CAFOS)
56005.63	292.63	Grism 4	3200-9100	355	16.2	NOT (ALFOSC)
56013.14	300.14	R600B	?-?	...	5.7	WHT (ISIS)
56013.14	300.14	R316R	?-?	...	3.0	WHT (ISIS)
56071.56	358.56	R500B	3440-7600	322	15.0	GTC (OSIRIS)
56072.61	359.61	R500R	4800-10000	352	20.8	GTC (OSIRIS)
56128.47	415.47	R300B	3600-7000	270	16.7	GTC (OSIRIS)

Table 9. Pseudo-bolometric 3-300 days UV to MIR lightcurve for SN 2011dh calculated from spectroscopic and photometric data with a 1-day sampling between 3 and 50 days and a 5-day sampling between 50 and 300 days. Random errors are given in the first parentheses and systematic lower and upper errors (arising from the distance and extinction) respectively in the second parentheses.

JD (+2400000) (d)	Phase (d)	L (log erg s^{-1})	JD (+2400000) (d)	Phase (d)	L (log erg s^{-1})
55717.00	4.00	41.465 (0.001) (0.098,0.186)	55773.00	60.00	41.670 (0.002) (0.093,0.160)
55718.00	5.00	41.553 (0.001) (0.097,0.181)	55778.00	65.00	41.627 (0.002) (0.093,0.160)
55719.00	6.00	41.653 (0.001) (0.097,0.179)	55783.00	70.00	41.585 (0.002) (0.093,0.161)
55720.00	7.00	41.747 (0.001) (0.097,0.178)	55788.00	75.00	41.544 (0.002) (0.093,0.161)
55721.00	8.00	41.835 (0.001) (0.097,0.178)	55793.00	80.00	41.502 (0.002) (0.093,0.161)
55722.00	9.00	41.909 (0.001) (0.097,0.178)	55798.00	85.00	41.460 (0.002) (0.093,0.162)
55723.00	10.00	41.970 (0.001) (0.097,0.177)	55803.00	90.00	41.417 (0.002) (0.094,0.162)
55724.00	11.00	42.019 (0.001) (0.097,0.176)	55808.00	95.00	41.375 (0.002) (0.094,0.163)
55725.00	12.00	42.057 (0.001) (0.097,0.176)	55813.00	100.00	41.333 (0.002) (0.094,0.163)
55726.00	13.00	42.089 (0.001) (0.096,0.175)	55818.00	105.00	41.291 (0.002) (0.094,0.163)
55727.00	14.00	42.118 (0.001) (0.096,0.174)	55823.00	110.00	41.249 (0.001) (0.094,0.164)
55728.00	15.00	42.142 (0.001) (0.096,0.174)	55828.00	115.00	41.208 (0.001) (0.094,0.164)
55729.00	16.00	42.164 (0.001) (0.096,0.173)	55833.00	120.00	41.166 (0.001) (0.094,0.164)
55730.00	17.00	42.182 (0.001) (0.096,0.173)	55838.00	125.00	41.124 (0.001) (0.094,0.164)
55731.00	18.00	42.198 (0.001) (0.096,0.173)	55843.00	130.00	41.081 (0.002) (0.094,0.164)
55732.00	19.00	42.209 (0.001) (0.096,0.172)	55848.00	135.00	41.038 (0.002) (0.094,0.165)
55733.00	20.00	42.214 (0.001) (0.096,0.172)	55853.00	140.00	40.995 (0.001) (0.094,0.165)
55734.00	21.00	42.216 (0.001) (0.096,0.171)	55858.00	145.00	40.953 (0.001) (0.094,0.165)
55735.00	22.00	42.211 (0.001) (0.095,0.171)	55863.00	150.00	40.909 (0.001) (0.094,0.165)
55736.00	23.00	42.201 (0.001) (0.095,0.170)	55868.00	155.00	40.863 (0.001) (0.094,0.165)
55737.00	24.00	42.186 (0.001) (0.095,0.169)	55873.00	160.00	40.817 (0.001) (0.094,0.165)
55738.00	25.00	42.165 (0.001) (0.095,0.167)	55878.00	165.00	40.772 (0.001) (0.094,0.165)
55739.00	26.00	42.142 (0.001) (0.094,0.166)	55883.00	170.00	40.726 (0.001) (0.094,0.164)
55740.00	27.00	42.117 (0.001) (0.094,0.165)	55888.00	175.00	40.681 (0.001) (0.094,0.164)
55741.00	28.00	42.091 (0.001) (0.094,0.164)	55893.00	180.00	40.637 (0.001) (0.094,0.164)
55742.00	29.00	42.064 (0.001) (0.094,0.163)	55898.00	185.00	40.594 (0.001) (0.094,0.164)
55743.00	30.00	42.039 (0.001) (0.094,0.162)	55903.00	190.00	40.552 (0.001) (0.094,0.164)
55744.00	31.00	42.016 (0.001) (0.093,0.162)	55908.00	195.00	40.512 (0.001) (0.094,0.164)
55745.00	32.00	41.996 (0.001) (0.093,0.161)	55913.00	200.00	40.472 (0.001) (0.094,0.164)
55746.00	33.00	41.977 (0.001) (0.093,0.161)	55918.00	205.00	40.432 (0.001) (0.094,0.164)
55747.00	34.00	41.959 (0.001) (0.093,0.160)	55923.00	210.00	40.396 (0.001) (0.094,0.164)
55748.00	35.00	41.943 (0.001) (0.093,0.160)	55928.00	215.00	40.362 (0.001) (0.094,0.164)
55749.00	36.00	41.928 (0.001) (0.093,0.160)	55933.00	220.00	40.327 (0.001) (0.094,0.164)
55750.00	37.00	41.914 (0.001) (0.093,0.159)	55938.00	225.00	40.294 (0.001) (0.094,0.164)
55751.00	38.00	41.900 (0.001) (0.093,0.159)	55943.00	230.00	40.262 (0.001) (0.094,0.164)
55752.00	39.00	41.887 (0.001) (0.093,0.159)	55948.00	235.00	40.230 (0.001) (0.094,0.164)
55753.00	40.00	41.874 (0.001) (0.093,0.159)	55953.00	240.00	40.200 (0.001) (0.094,0.163)
55754.00	41.00	41.861 (0.001) (0.093,0.159)	55958.00	245.00	40.169 (0.001) (0.094,0.163)
55755.00	42.00	41.848 (0.001) (0.093,0.159)	55963.00	250.00	40.137 (0.001) (0.094,0.163)
55756.00	43.00	41.836 (0.001) (0.093,0.159)	55968.00	255.00	40.104 (0.001) (0.094,0.163)
55757.00	44.00	41.823 (0.001) (0.093,0.159)	55973.00	260.00	40.071 (0.001) (0.094,0.163)
55758.00	45.00	41.812 (0.001) (0.093,0.159)	55978.00	265.00	40.039 (0.001) (0.094,0.163)
55759.00	46.00	41.802 (0.001) (0.093,0.159)	55983.00	270.00	40.006 (0.001) (0.094,0.163)
55760.00	47.00	41.792 (0.001) (0.093,0.159)	55988.00	275.00	39.973 (0.001) (0.094,0.163)
55761.00	48.00	41.782 (0.001) (0.093,0.159)	55993.00	280.00	39.940 (0.001) (0.094,0.163)
55762.00	49.00	41.773 (0.002) (0.093,0.159)	55998.00	285.00	39.907 (0.001) (0.094,0.163)
55763.00	50.00	41.763 (0.002) (0.093,0.159)	56003.00	290.00	39.873 (0.001) (0.094,0.163)
55768.00	55.00	41.716 (0.002) (0.093,0.159)	56008.00	295.00	39.838 (0.001) (0.094,0.163)